FY08 JOINT FACILITY RESEARCH JOULE MILESTONE FINAL REPORT

by
DIII-D, C-Mod, and NSTX Research Teams

Prepared for
the U.S. Department of Energy under
DE-FC02-04ER54698, DE-AC02-76CH03073,
and DE-FC02-99ER54512

SEPTEMBER 2008

DISCLAIMER

DESCRIPTION OF DELIVERABLE

Conduct experiments on major fusion facilities leading toward the predictive capability for burning plasmas and configuration optimization. In FY 2008, FES will evaluate the generation of plasma rotation and momentum transport, and assess the impact of plasma rotation on stability and confinement. Alcator-Mod will investigate rotation without external momentum input, NSTX will examine very high rotation speeds, and DIII-D will vary rotation speeds with neutral beams. The results achieved at the major facilities will provide important new data for estimating the magnitude of and assessing the impact of rotation on ITER plasmas.

DEFINITION OF COMPLETION

Complete the required experiments and prepare a joint report summarizing the data and analysis contributing to estimating the magnitude, and assessing the impact, of rotation on ITER.

CONTENTS

CONTENTS (Continued)

CONTENTS (Continued)

CONTENTS (Continued)

LIST OF FIGURES

LIST OF FIGURES (Continued)

LIST OF FIGURES (Continued)

LIST OF FIGURES (Continued)

LIST OF FIGURES (Continued)

INTRODUCTION & EXECUTIVE SUMMARY

1. COMPLETION OF THE MILESTONE

All three facilities successfully executed their planned operatioNnal run periods and devoted a large fraction of the experimental effort to experiments that supported completion of the FY08 JOULE FES milestone. In Appendix A we give the final list of experiments for all three facilities, indicating synergistic connections, and providing the experimental number designations unique to each facility. Much more detail can be found on each experiment by using the weblinks to each facility given in Appendix A. Additionally, some publications have appeared and others are in progress that are directly a result of the FY08 JOULE FES milestone research at the three facilities. These are listed in Appendix B, and called out in the detailed sections of this report.

As stated in the Annual Target, the impact of toroidal plasma rotation in the tokamak cuts across many areas of science important for ITER, and consequently, cross-disciplinary rotation focused experimental teams were formed at each facility. The ability to confidently project the magnitude of rotation in ITER has design impact for issues related to stability and confinement. Both neoclassical tearing mode (NTM) and the resistive wall mode (RWM) instabilities are ameliorated by rotation, and ITER is planning active systems to stabilize each, electron cyclotron current drive (ECCD) and fast response feedback coils, respectively. Local transport is known to be reduced by shear in the rotation profile. Thus, the specifications on auxiliary heating systems, and the ultimate energy content of a burning plasma (BP) could depend upon the rotation profile. This profile will be determined by the momentum sources, the momentum transport processes and possible internal momentum sinks, usually produced by errors in the magnetic field configuration, which cannot be completely eliminated but can be reduced so as not to effect performance. It is around these general considerations, stability, confinement, and the momentum equation itself that we have organized the experimental plan, and this report on the results. We will speak of rotation and toroidal velocity somewhat interchangeably, since these are closely related quantities.

In FY08 Alcator C-Mod continued investigation of rotation without external momentum input, utilizing a new imaging high-resolution x-ray spectrometer. Active flow drive using ICRF mode converted waves has been demonstrated, with observed co-current toroidal rotation velocities in excess of 100 km/s, in addition to substantial core poloidal rotation. These results compare favorably with theory and extrapolation to ITER suggests rotation velocities of hundreds of km/s may be possible. During lower hybrid current drive (LHCD) experiments, strong central counter-current toroidal rotation has

been observed, which is consistent with an inward shift of fast electron orbits. LHCD has been successfully added to ICRF H-mode discharges and velocity profile shape control has been demonstrated. Evidence of an inward momentum pinch has been seen in ICRF H-mode plasmas. The intrinsic rotation database continues to be populated and extrapolation to ITER is favorable. A novel rapid shape change experiment was developed to follow the subsequent transport of the intrinsic momentum profile. C-Mod also performed high resolution velocity measurements in the H-mode pedestal region that are important regarding identification of the possible source of intrinsic rotation. A similarity experiment was conducted with the Swiss tokamak, TCV, to duplicate an inversion of the intrinsic rotation direction with high density.

NSTX examined rotation effects at very high rotation speeds in FY08, including sources, transport, sinks and the effect upon stability and confinement. Non-resonant magnetic perturbations and modulated neutral beam injection (NBI) were used in momentum transport experiments, where a momentum pinch effect is clearly needed to explain the measurements in the outer region of the plasma. NSTX continued their experimental efforts on nonresonant magnetic perturbations, typically a sink for momentum but which in some sense can be considered a source due to the prediction of an offset rotation, in the theory of neoclassical toroidal viscosity (NTV). The benefit of reducing even nonresonant magnetic error fields was clearly shown in another NSTX experiment, related to momentum sinks. The stability threshold for tearing modes in NSTX is shown to depend upon rotation, and rotation shear, in experiments this year. Regarding the impact of rotation upon stability of the RWM, NSTX experiments show that there is a dependence on the collisionality regime in the plasma. And NSTX also used magnetic braking to demonstrate the benefit or rotation and rotation shear upon energy confinement.

DIII-D executed experiments utilizing the capability to vary rotation speeds and direction by controlling the mix of co-Ip and counter-Ip injected torque. Balanced NBI was utilized to investigate the intrinsic rotation scaling to higher levels of normalized plasma energy, β_N. A model for the resonant rotation boundary condition emerged from pedestal velocity measurements in DIII-D. Modulated NBI torque experiments were done for momentum transport, and the results were compared with those from NSTX. DIII-D clearly identified the NTV offset velocity in a series of nonresonant magnetic perturbation experiments. Resonant magnetic perturbation experiments unified results in low and high β_N plasmas by considering the resonant response in the plasma. The experiments on NTM stability due to rotation and rotation shear were also done in part collaboratively with NSTX. DIII-D did an experiment to compare rotation shear with magnetic shear regarding energy confinement. The power threshold to achieve the H-mode confinement regime was carefully mapped out as a function of rotation, for both

deuterium and hydrogen plasmas. And the quiescent H-mode regime (QH), free of edge localized modes (ELMs), was for the first time achieved with co-Ip rotation.

For a brief description of the experimental highlights, we start with the generation of rotation and move to the impact issues of stability and confinement. Significant progress was made in every area with the experiments in FY08. Completely new phenomena were discovered and indications from former experiments were confirmed and extended. Common underlying physics elements controlling the rotation dynamics and momentum transport were identified among the three experiments, which covered a wider range of parameter space than could be accomplished by combinations of any one or two. Greater coupling with theory was also accomplished, giving increased confidence for extrapolation to ITER and BPs in general.

2. HIGHLIGHTS

2.1. ROTATION GENERATION

2.1.1. RF Flow Drive

Two completely new rotation control phenomena were discovered this year, each due to methods utilizing RF heating of the plasma. Each of these appears to have connection to theory and as such can be extrapolated to ITER. The first is the use of the well-known process of mode conversion (MC) of a launched fast magnetosonic wave into a slow ion cyclotron wave (ICW). This process was suggested theoretically over thirty years ago and in recent years has been studied theoretically as a tool to generate flow in the plasma. This experiment is the first to clearly demonstrate the ability to generate a significant toroidal rotation, to make direct comparisons with standard ion cyclotron resonant heating (ICRH) and find that theory aptly describes the results. The ITER start-up design calls for a 20MW RF heating system that can be directly used to produce this effect. The projected level of toroidal rotation would be very significant in ITER (see Sec. 3.1), using the standard of comparing the toroidal velocity, V_ϕ, with the Alfven velocity, V_A, or the ion thermal velocity, V_{th}.

In the second, lower hybrid current drive (LHCD) was found to produce a toroidal rotation in the direction opposite to that of the plasma current, Ip. That is, the driven V_ϕ is in the counter-Ip direction. Only one direction of current drive has a significant effect, and it produces this rotation. The explanation proposed is that the RF-wave oscillating electric field which drives the electron current also produces a radial pinch of fast electrons. This pinch generates a small, but significant radial current in the plasma that produces a negative electric field in the core, and hence the counter-Ip rotation. This radial current is driven by a wave resonant version of the well-established Ware pinch. This hypothesis will be directly testable with existing codes and if borne out will provide a direct prediction for ITER, where the upgrade design incorporates 20MW of LHCD.

The mode conversion current drive (MCFD) experiment produced a rotation in the direction of Ip, that is, V_ϕ is co-Ip there. It may be possible to generate enhanced local sheared flow in combination with LHCD and thereby enhance locally the thermal insulation of the plasma.

These two experiments are discussed in Sec. 3 on Intrinsic Rotation because the mechanisms do not utilize the standard momentum source due to neutral beam injection (NBI), but, rather that due to momentum inherent in the RF wave itself.

2.1.2. Intrinsic Rotation

Intrinsic rotation occurs without auxiliary input of torque to the plasma. Indications are that the source may be at the edge, and the momentum is transported inward convectively, with a so-called momentum pinch, coming to steady state after being balanced by outward diffusive momentum transport.

Balanced NBI was used to probe the empirical intrinsic rotation scaling at higher levels of normalized plasma stored energy, specified by the β_N parameter. The database of international tokamak results on intrinsic rotation in rf heated plasmas has very few points with β_N greater than 1.25. ITER-relevant values set in for $\beta_N > 1.7$. In these FY08 experiments β_N has been extended to values > 2.0 under conditions that allow study of the intrinsic rotation. Although there is no inconsistency between these results and the empirical scaling laws developed to date, allowance must be made for a reduction in the momentum confinement time due to NTMs, or energetic fast ion instabilities, both of which accompanied operation at the higher β_N values. A large amount of data was acquired in these experiments and must be analyzed to draw a final conclusion.

A similarity experiment was done with the Swiss tokamak, TCV. The inversion of the sign of the intrinsic toroidal velocity with increasing plasma density seen in TCV was duplicated in non-diverted L-mode conditions. This is an important demonstration of the universality of this particular effect. A sign change is a very strong signature and hopefully lead to identification of the nature of the presumed turbulent drive in low density, and high density.

If we continue to use the scaling laws for intrinsic rotation derived from engineering parameter fits to the international database we find that even the most pessimistic law produces a value of intrinsic rotation in ITER, of order a few hundred km/sec in toroidal velocity. This is significant when scaled to the Alfvén or ion thermal velocities.

2.2. MOMENTUM TRANSPORT

Perturbative techniques have been used to develop a more comprehensive picture of momentum transport than can be determined with steady-state analysis. This allows more direct connection with theory. External torque perturbations that were used include use of NBI pulses, braking pulses from applied magnetic fields, and rapid changes to the plasma boundary shape.

The results show that a description of momentum transport using only an effective diffusivity is inadequate, and that a momentum pinch is indicated, with values of the pinch velocity up to 40 km/sec. This result is robust, and independent of aspect ratio. The source of the pinch appears to be tied to low-k turbulence, as predicted by some theories.

With quantitative theoretical determination of the momentum diffusivity and pinch velocity the rotation profile can be specified in ITER, given a known torque source. ITER will have NBI of 33 MW in the start-up phase, with a known torque input. ITER simulations for the NBI-driven velocity without a momentum pinch give a relatively low velocity compared to those mentioned in the above effects. The inclusion of a momentum pinch in the modeling will increase this velocity prediction and the experiments done here will be important to project the level of pinch expected in ITER.

With known momentum transport coefficients the ITER steady-state velocity for a known RF-induced flow drive (Secs. 3.1 and 3.2), or intrinsic rotation resulting from a nonzero boundary value (Sec. 6) can also be projected. It appears that the momentum pinch effect can result in increasing the projected ITER rotation to significant levels and must be thoroughly understood.

2.3. MOMENTUM SINKS

The important momentum sinks are those due to magnetic perturbations that break the axisymmetry of the toroidal geometry. These are divided into the more benign nonresonant perturbations, and the resonant perturbations that produce a dramatic braking of toroidal rotation. This has become a very important topic for ITER since the discovery that edge-resonant magnetic perturbations can stabilize ELMs. Accompanying these edge resonant components are components that are nonresonant in the interior of the plasma.

For nonresonant perturbations, experiments continue to validate recent theoretical work that describes the interaction on rotation as Neoclassical Toroidal Viscosity (NTV). The NTV effect result can produce a steady state nonzero velocity in the counter-Ip direction. This offset velocity has been clearly identified in experiments this year. That is, an error field can be used to generate a nonzero toroidal rotation in some circumstances, rather than always a damping of rotation. NTV theory also predicts that the rotational damping term will become stronger at lower collisionality, i.e. in ITER conditions. Experiments this year have verified the collisionality effect through variations in ion temperature.

Tokamaks employ added magnetic coils to trim out unwanted error fields, and ITER will likely do so also. Usually the resonant $n = 1$ error perturbations are of most concern, where n is the toroidal mode number. However, experiments have shown that higher-n error fields can be just as important, and that correcting the additional nonresonant error fields can lead to enhanced operational space.

For resonant magnetic perturbations an experiment has shown the necessity to account for the plasma response in understanding the dynamics of the strong toroidal rotation damping, and ultimately locking, which often leads to disruption. The plasma response to these perturbations results from internal magnetic field generation due to

perturbation-driven currents within the plasma flowing on the resonant surfaces. This picture unifies observations in two very different regimes, one in very low β_N cold plasmas, and the other in high β_N plasmas at or beyond a stability limit. The low density limit in the former, and the β_N limit in the latter are found to be described by greater plasma response as the limit is approached.

2.4. BOUNDARY CONDITION

The boundary condition on rotation, that is, the velocity at the boundary plasma surface, is important to understand in order for any theory to project an absolute rotation profile for ITER. H-mode plasmas are the relevant mode of operation so the pedestal region is considered for mechanisms that could establish a robust boundary condition for intrinsic velocity.

A signature of the pedestal is the deep, localized negative well in the radial electric field. Such a localized structure, narrower than a typical trapped ion drift orbit width, could result in rotation in the pedestal. Experiments this year probed this well structure width in very high spatial resolution, and identified the poloidal flow as an important term in maintaining this electric field.

In other work it was noted that the measured intrinsic toroidal velocity in the pedestal region is approximately proportional to the local ion temperature. This result is consistent with a simple model of thermal ion orbit loss where only ions flowing in one direction are preferentially lost. Applying this model to the projected ITER pedestal conditions for the initial inductive H-mode operation gives a co-Ip toroidal velocity of approximately 8 km/sec at the top of the pedestal. This would not be considered large in a device the size of ITER, producing a rotation frequency of less than 200 Hz, but coupled with the momentum pinch effect the internal intrinsic rotation rate could become significant with just such an edge source.

2.5. EFFECTS OF ROTATION – STABILITY

A wide variety of magnetohydrodynamic (MHD) instabilities has been shown to be modified strongly by rotation and/or rotation shear. Both $m = 2/n = 1$ and 3/2 NTMs have increased stability at larger rotation and rotation shear, where m is the poloidal mode number. Shear in the magnetic field also is found to affect stability.

Results suggest that in ITER the resistive wall mode (RWM) instability may be stabilized by eddy currents in the surrounding wall at very low plasma rotation, as long as driving perturbations, such as error fields, or ELM perturbations, can be sufficiently mitigated. Active feedback stabilization techniques are also used to limit RWM growth. The detailed physics of rotation stabilization continues to be revealed through a very successful experimental multi-machine effort.

2.6. EFFECTS OF ROTATION – CONFINEMENT

Various techniques have been employed to vary the $E \times B$ velocity shear, as well as the magnetic shear, and relate these to variations in transport and turbulence. These techniques include $n = 3$ magnetic braking, the mix of co-Ip and counter-Ip NBI, and ramping the plasma current at different rates. The results are consistent with the model that reduced transport results from $E \times B$ shear suppression of low-k turbulence, as seen in theoretical linear gyrokinetic calculations. Magnetic shear is also found to be important for optimizing confinement in any BP, including ITER.

2.7. EFFECTS OF ROTATION – THE L -> H POWER THRESHOLD

The power required to enter the H-mode confinement regime is found to depend upon the toroidal rotation, with higher values of co-Ip rotation requiring higher power for transition. This is a positive result for ITER, where the rotation level is projected to be relatively smaller than that in today's experiments with strong uni-directional NBI torque. However, the power required to achieve a transition in hydrogen plasmas, H^+, is found to be higher than in deuterium, D^+, plasmas. Unless techniques are developed to overcome this it could be an issue for ITER operation in the early, non-activation phase.

2.8. EFFECTS OF ROTATION – QH MODE

The Quiescent H-mode (QH) is an advanced confinement mode of operation free of ELMs, which must be avoided for longevity in ITER. Previously, QH modes were only found in discharges with sufficient counter-Ip NBI. In 2008 this limit was overcome, and QH-mode was achieved with dominant co-Ip NBI, and resulting co-Ip toroidal rotation throughout the plasma. This newly discovered regime is consistent with theoretical predictions, which relate the edge region velocity shear with the properties of the Edge Harmonic Oscillation (EHO). The EHO mode accompanies QH-mode and is believed to provide a necessary level of particle transport that holds the pedestal pressure below the instability threshold.

3. INTRINSIC CORE ROTATION

3.1. MODE CONVERSION FLOW DRIVE

3.1.1. Overview

For the first time in tokamaks, significant toroidal flow driven by the ICRF mode conversion (MC) process has been observed in C-Mod. In the past, the direct launch of RF to generate ion Bernstein waves was used to generate a flow [1]. Now RF in the frequency range to be installed in ITER has been shown to undergo MC to these shorter wavelength modes in the plasma. The flow is in both the toroidal and poloidal direction, known to be valuable for increased plasma stability, and increased energy confinement due to velocity shear, respectively. The results are understandable from nonlinear rf wave theory and thus can be extrapolated to ITER.

Additional details will appear in the publication cited in Appendix B.1.

3.1.2. Experimental Results

The central rotation velocity $V_\phi(r=0)$ of two upper-single-null plasmas in L-mode with the same electron density but with different ICRF applications is compared in Fig. 3.1: one using the 80 MHz wave in dipole phasing (minority heating, MH), and the other using the 50 MHz wave (MC) phased at +90° (i.e., wave traveling in the co-current direction). The toroidal flow velocity, derived from the Doppler shifts of the x-ray spectra of Ar^{17+} impurity ions measured by high resolution x-ray spectroscopy, is significantly higher in the MC plasma than that in the MH plasma. In the MC plasma, $V_\phi(r=0)$ rises from -10 km/sec (counter-Ip direction), a typical value in Ohmic L-mode plasmas, to +75 km/sec ($M_A = V_\phi / V_A \sim 0.014$, where M_A is the Alfvén Mach number and C_A is the Alfvén velocity) in the co-current direction with 3 MW of ICRF power. The velocity change ΔV_ϕ is approximately linear vs. P_{rf}, indicating a mechanism where rf power dissipation is important, rather than a mechanism directly related to the rf field strength. In contrast, in the MH plasma at approximately the same P_{rf} and heating history as the MC plasma, $V_\phi(r=0)$ only rises to +20 km/sec. Strong co-current rotation has been observed in many MC plasmas where $5.0 < B_t < 5.2$ T and with both the ion cyclotron (IC) resonance and MC surface near the magnetic axis. When compared with the empirically determined intrinsic rotation scaling law, the Rice scaling [2,3], $\Delta V_\phi \sim \Delta W_p / I_p$, the rotation change in these MC plasmas is generally a factor > 2 larger than that from MH plasmas with identical plasma shape, magnetic field, current and density.

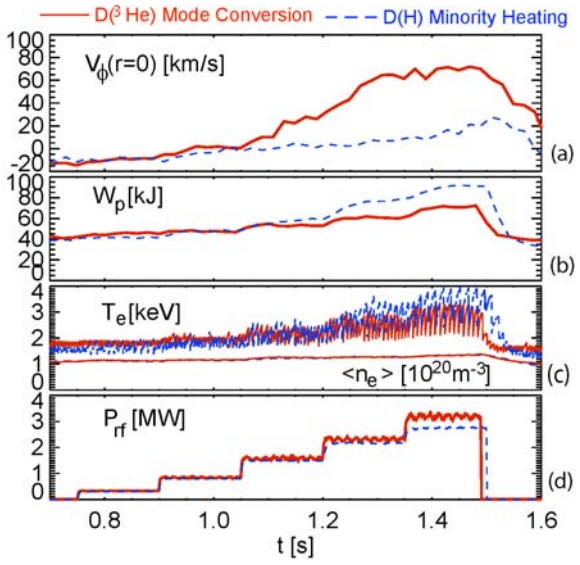

Fig. 3.1. Parameter time histories for MC (red) and MH (blue) discharges. C-Mod.

Unlike the intrinsic toroidal rotation, which propagates inward from the edge through momentum pinch and diffusion, the toroidal rotation in MC plasmas rises first near the plasma center. In Fig. 3.2 the time traces of ΔV_ϕ at $r/a \sim 0$, 0.3 and 0.7 of a MC plasma are compared. Both velocities at $r/a = 0$ and 0.3 rise to a steady value in less than 80 ms after the application of the 50 MHz rf power, while $\Delta V_\phi(r/a \sim 0.7)$ is delayed and with a much smaller magnitude. The difference in the response to rf power also creates a broad centrally peaked V_ϕ profile in MC plasmas. In Fig. 3.3(a), the chord integrated rotation profiles obtained from Ar^{16+} of the two plasmas in Fig. 3.1 are compared. V_ϕ profiles before the rf application at $t = 0.7$ s are both flat. When heated with the rf power at $t = 1.4$ s, the rotation profile in the MH plasma is flat to slightly hollow. In contrast, $V_\phi(r/a)$ of the MC plasma is broadly peaked within $r/a < 0.5$, but at a similar level to that of the MH plasma in the outer region $(r/a > 0.5)$. In Fig. 3.3(b), the Ar^{16+} ion temperature profiles show that the MC plasma has a higher T_i than that of the MH plasma for $r/a < 0.5$, while has a somewhat lower T_e as seen in Fig. 3.1(c).

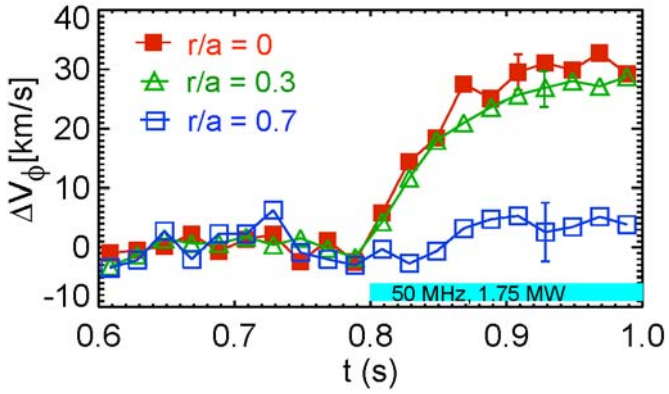

Fig. 3.2. Toroidal rotation velocity time histories at three radii for a MC plasma. C-Mod.

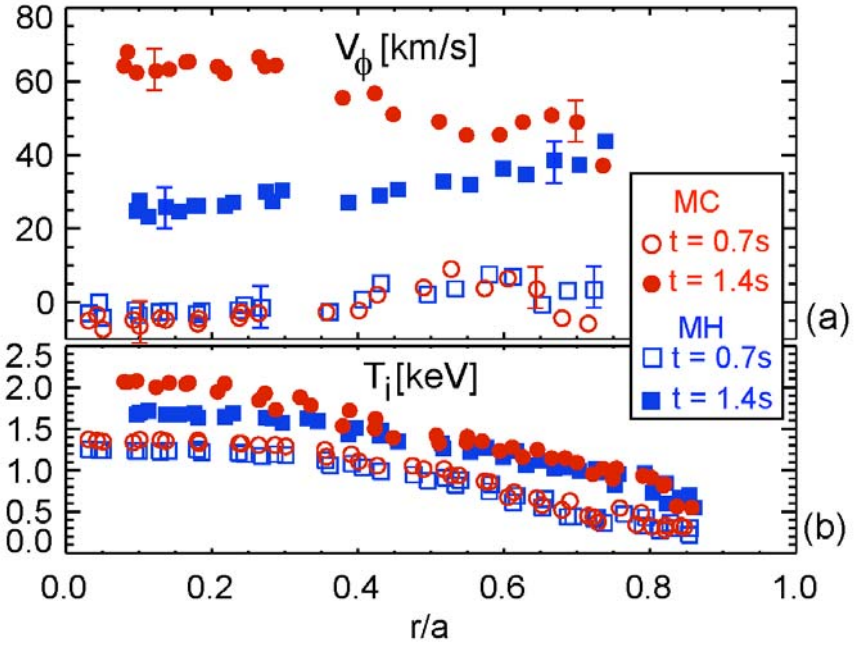

Fig. 3.3. Toroidal rotation (top) and ion temperature (bottom) profiles for MC (red) and MH (blue) plasmas. C-Mod.

Concomitant to the strong toroidal rotation, a poloidal flow V_θ in the ion diamagnetic direction is observed in the MC plasma. In Fig. 3.4, $\Delta V_\theta(r/a)$ at different rf power levels in the MC and MH plasmas are compared. In the MH plasma, there is no detectable poloidal flow, while in the MC plasma, a significant flow appears in the region of $0.3 < r/a < 0.5$, and peaks at ~ 0.7 km/s per MW rf power. In Fig. 3.5(b), the peak poloidal velocity $\Delta V_\theta(r/a = 0.44)$ is plotted vs. time, and it shows that the flow becomes significant when $P_{rf} > 1.5$ MW and increases with P_{rf} (Fig. 3.5(c)). Interestingly, the density fluctuation spectra of Fig. 3.5(a), measured by a phase contrast imaging (PCI)

system, show a turbulence frequency broadening following the same trend as V_θ indicating a change in bulk ion flow as well.

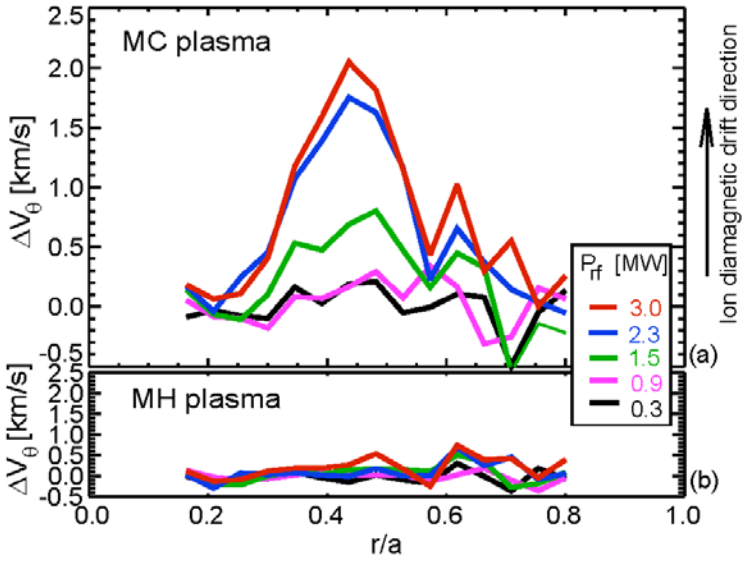

Fig. 3.4. Poloidal rotation profiles for MC (top) and MH (bottom) plasmas. C-Mod.

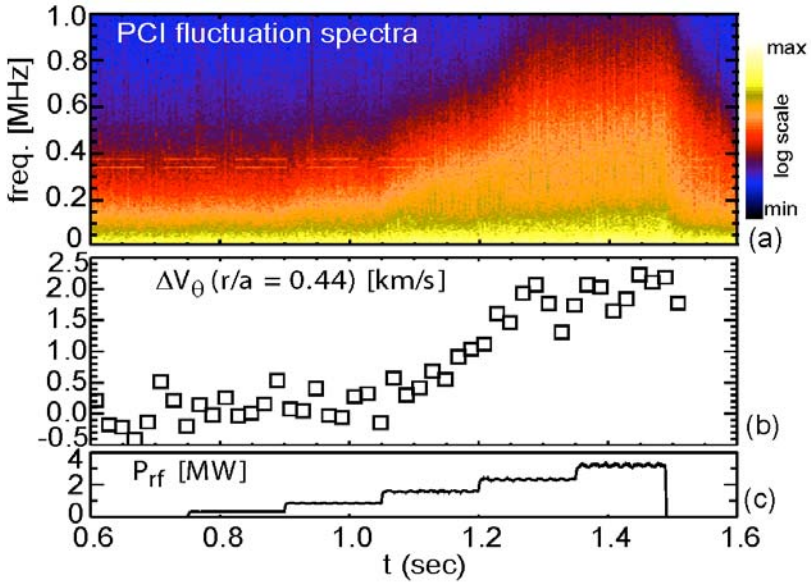

Fig. 3.5. Turbulence spectrum (top) and poloidal rotation velocity (bottom) for a MC plasma. C-Mod.

3.1.3. Comparison with Theory

On C-Mod, fast waves at 80 MHz and 50 MHz are launched externally from the low field side (LFS), either separately or combined. The 80 MHz fast wave heats the plasma via D(H) minority heating (MH) with residual $n_H/n_e < 5\%$. The fast wave power is first

deposited to the minority H ions via ion cyclotron (IC) resonance, $R_{IC,H} \sim 0.65$ m, slightly on the high field side (HFS) of the magnetic axis, and then the energetic H ions transfer their energy to the bulk electrons and majority deuterium ions when they slow down through collisions. In D–^{3}He plasmas with moderate ^{3}He concentration, the 50 MHz fast wave $\left(R_{IC,3\mathrm{He}} \sim 0.71 \text{ m}\right)$ can be mostly converted to short wavelength slow waves, ICW and ion Bernstein waves (IBW), near the MC surface (also called D–^{3}He hybrid layer), and directly heat electrons and ions.

The two-dimensional (2-D) full-wave code TORIC [4] has been used to simulate the MC plasma. The species mix in the simulation is iteratively determined to be $n_{3\mathrm{He}}/n_e = 8\%$ so that the peak electron deposition matches. The location of the MC wave field also matches that from the PCI wave measurement. The total electron deposition from the simulation is 0.6 MW out of 3 MW, and 2.2 MW of the power is absorbed by the ^{3}He ions, with the rest to D ions.

From the TORIC simulation, the power deposition to the ^{3}He ions is mostly through the MC ICW, rather than through the fast wave like in MH plasmas. In Fig. 3.6, the 2-D power deposition profiles from the TORIC run with $n_\phi = +6$ are shown. In Fig. 3.6(a), the ion deposition by the MC ICW is shown to be more than an order of magnitude larger than that by the FW. Fig. 3.6(b) shows a weak electron deposition by the MC ICW but strong electron heating by the MC IBW on the HFS of the MC layer. The MC ICW deposition is within several cm on the LFS of the MC layer, and strongest at $\sim 7-12$ cm vertically below and above the mid-plane, where a larger poloidal B field makes the mode conversion to ICW possible. These peak deposition regions map to the flux surfaces of $0.3 < r/a < 0.5$, the same location where local poloidal flow is observed. Numerically solving the full electromagnetic wave dispersion equation finds that the ICW $k_{||}$ is up-shifted from the FW level of 10 m^{-1} to $k_{||} \sim 40 \sim 50$ m^{-1}, and the IC resonance condition $\omega \sim \Omega_{c,3\mathrm{He}} + k_{||} v_{t,3\mathrm{He}}$ can be satisfied in the vicinity of the MC surface, about 4 cm away on the HFS of the IC resonance. This is consistent with the TORIC simulation showing that significant ion damping of the ICW occurs near the MC surface.

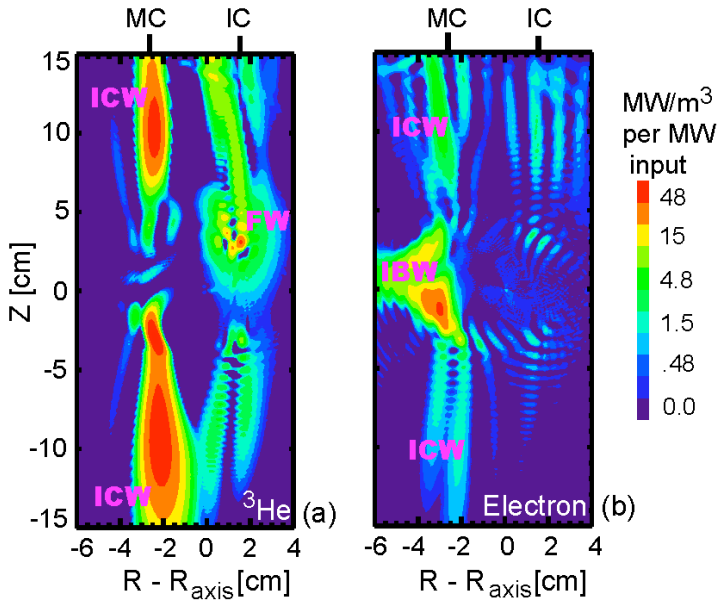

Fig. 3.6. Ion (left) and electron (right) power deposition from TORIC. C-Mod.

The involvement of slow wave and resonant wave-ion interaction is consistent with previous theoretical work on rf flow drive. Analytical estimates for V_ϕ and V_θ generated by direct-launch IBW at the diffusive limit are [5]

$$V_\phi[\text{km/s}] \sim 48 P_{rf}[\text{MW}] k_{||}[\text{m}^{-1}] \big/ R[\text{m}] f[\text{MHz}] D[\text{m}^2/\text{s}] n_{20} \mu \quad ,$$

$$V_\theta[\text{km/s}] \sim 0.4 P_{rf}[\text{MW}] \big/ q^2 R[\text{m}] r[\text{m}] B[\text{T}] D[\text{m}^2/\text{s}] n_{20} \quad .$$

Using the parameters of the MC plasma in Fig. 3.1, $B \sim 5.1\,\text{T}$, $n_{20} \sim 1.3$, $R \sim 0.7$ m, $r \sim 0.1$ m, $k_{||} \sim 40$ m^{-1}, $f = 50$ MHz, $\mu \sim 2.1$, $q \sim 1.6$, and L-mode momentum diffusion coefficient $D \sim 0.2$ m^2/s, we have $V_\theta \sim 100$ km/s and $V_\theta \sim 2$ km/s per MW. Assuming that the MC ICW (about half of the total input power) interacts with ions similarly to direct launch IBW, these estimates are comparable to our experimental observation.

3.2. LOWER HYBRID CURRENT DRIVE IN C-MOD

3.2.1. Overview

Self generated flows associated with lower hybrid current drive (LHCD) have been observed in both L-mode and H-mode discharges on Alcator C-Mod when lower hybrid waves are launched such as to drive positive current. These changes to the toroidal rotation profile are core localized ($r/a \sim < 0.4$) and always in the counter-current direction. When the waves are launched against the inductive toroidal electric field, very little current is driven and no effect on the rotation profile is observed. This result

indicates that it is the LHCD (as opposed to heating) that is responsible for the counter-current change in toroidal rotation. In discharges with sufficient LHCD, a region of high velocity shear forms concurrently with a negative increment in the radial electric field profile.

A possible explanation is a negative nonambipolar electric charging of the core due to a resonant trapped electron pinch, in analogy to the Ware pinch phenomenon. This pinch is the result of the canonical angular momentum absorbed by resonant trapped electrons while interacting with lower hybrid waves. If this proves correct with rf theory and modeling it will be straightforward to establish the type of system necessary for ITER to achieve a desired level of velocity shear.

Additional details will appear in the publications cited in Appendix B.2,3.

3.2.2. Experimental Results

Shown in Fig. 3.7 is the temporal evolution of selected parameters for an L-mode discharge in which the injection of lower hybrid waves caused a strong counter-current change in the toroidal rotation profile (solid lines). 600kW of lower hybrid power (with $n_{||} = 1.6$) are coupled to the plasma at $t = 0.8$ s. Immediately following the application of LH power, the central toroidal rotation began to evolve on a time scale considerably longer than the energy and momentum confinement times (~ 20 ms) but comparable to the current redistribution time ($\tau_{CR} = 1.4\kappa a^2 T_e^{1.5}(keV)/Z_{eff} \sim 150$ ms). The ability to sustain LHCD for many current redistribution times makes it possible to study the induced rotation in plasmas with fully relaxed current density profiles.

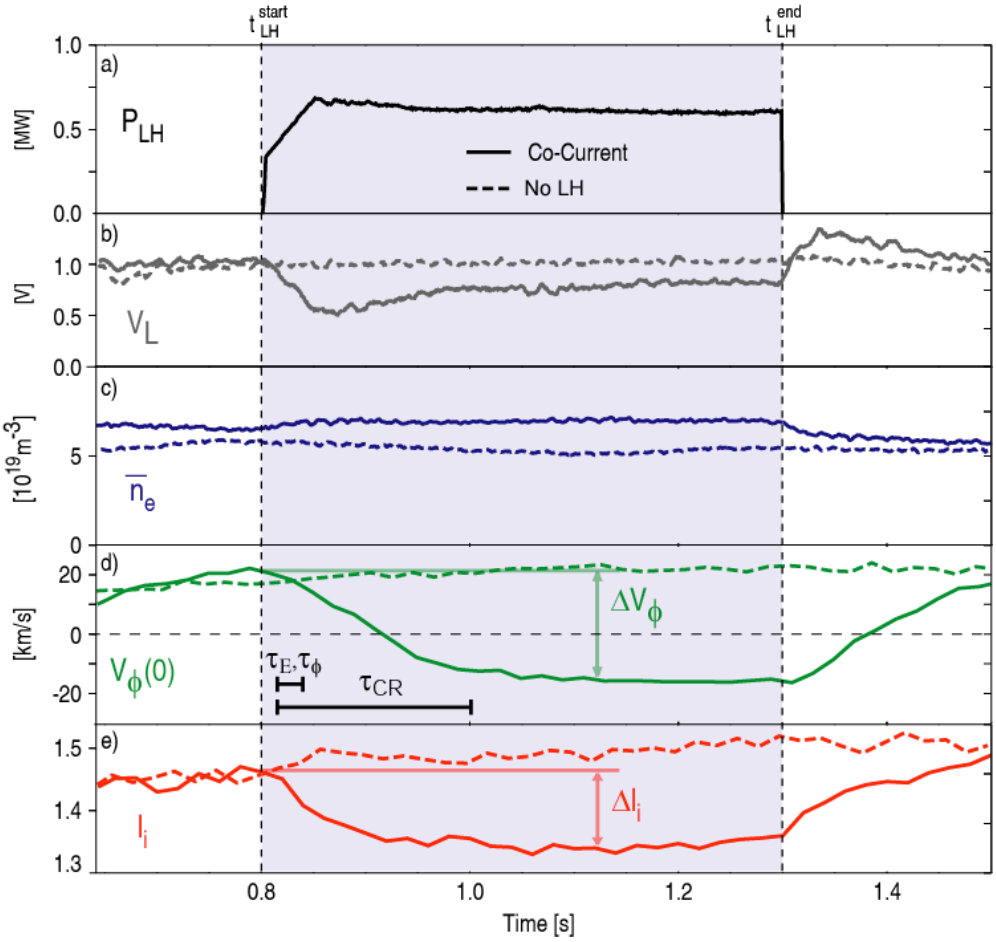

Figure 3.7. Time histories of a) lower hybrid power, b) loop voltage, c) line averaged density, d) central toroidal rotation velocity and e) the normalized internal inductance ℓ_i for discharges with LHCD (solid lines) and without LHCD (dashed lines). Both discharges had the same magnetic field (5.4 T) and plasma current (800 kA). C-Mod.

Modification of the toroidal rotation profile by LHCD has been observed over a range of electron densities, plasma currents, magnetic fields, and lower hybrid powers in C-Mod. Although the magnitude of the effect depends on these parameters, in every instance the change in toroidal rotation is in the counter-current direction. In discharges initially rotating in the co-current direction (as in Fig. 3.7) the application of LHCD can cause the rotation to change sign. While the precise mechanism by which the lower hybrid waves affect the rotation profile remains uncertain, rotation inversions such as these can not be explained solely by changes in viscous damping (an increase or decrease in viscous damping would change the magnitude of the flow but not its sign).

Also of interest is the change in normalized internal inductance, ℓ_i (a measure of the peaking in the current density profile, given by the ratio of the volume averaged to surface averaged poloidal magnetic energy). The motional Stark effect (MSE) diagnostic was not available for these discharges and as a result, knowledge of the current density

profile is limited to global quantities such as ℓ_i and changes in loop voltage. The decrease in ℓ_i between 0.8 s and 1.3 s indicates that the current density profile is broadening due to the off-axis current being provided by the lower hybrid waves. The quantity $\Delta\ell_i$ shown in Fig. 3.7 is defined as the change in the internal inductance relative to the start time of the LHCD pulse (ΔV is defined similarly). The clear correlation between $\Delta V_\phi(t)$ and $\Delta\ell_i(t)$ during the LHCD phase in Fig. 3.7 is seen in all LHCD discharges and provides further evidence of the relationship between LHCD and rotation profile modification. The correlation between changes in central toroidal rotation and normalized internal inductance is observed in a wide variety of plasmas. This is illustrated in Fig. 3.8 in which ΔV_ϕ and $\Delta\ell_i$ data are plotted for discharges with varying magnetic field, plasma current, density, magnetic topology, confinement regime, lower hybrid power and launched $n_{||}$.

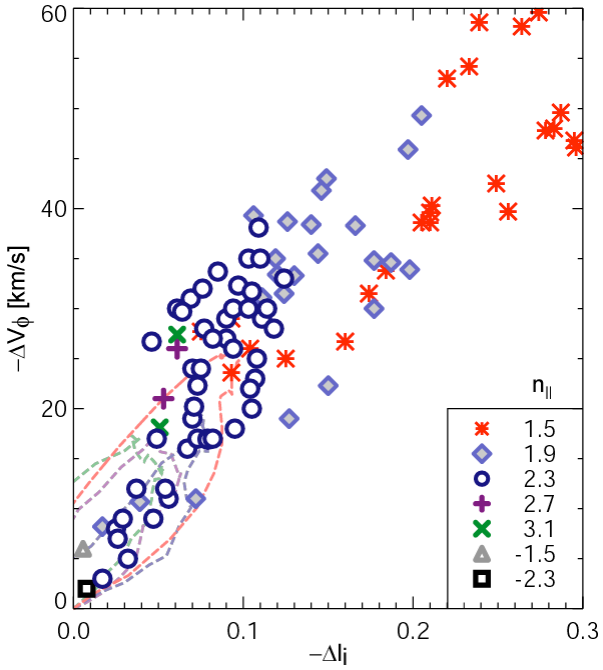

Fig. 3.8. LH induced changes in central toroidal rotation and normalized internal inductance for a wide variety of plasmas (Each point represents a single discharge). The trajectories from Fig. 3.8 (dashed lines) are included for comparison. C-Mod.

The modification of the toroidal rotation profile produced by LHCD tends to be core localized, with the largest changes occurring in the range $0 < r/a < 0.4$. The sawtooth-averaged radial profiles of n_e, V_ϕ, T_e, T_i and E_r both before and during the application of LHCD are shown in Fig. 3.9. The radial electric field, E_r, was calculated by measuring all terms in the radial force balance equation, with the dominant contribution coming from the toroidal rotation term. The change in the radial electric field profile indicates that there is a non-ambipolar radial current charging the plasma negatively with respect to its pre-LH state.

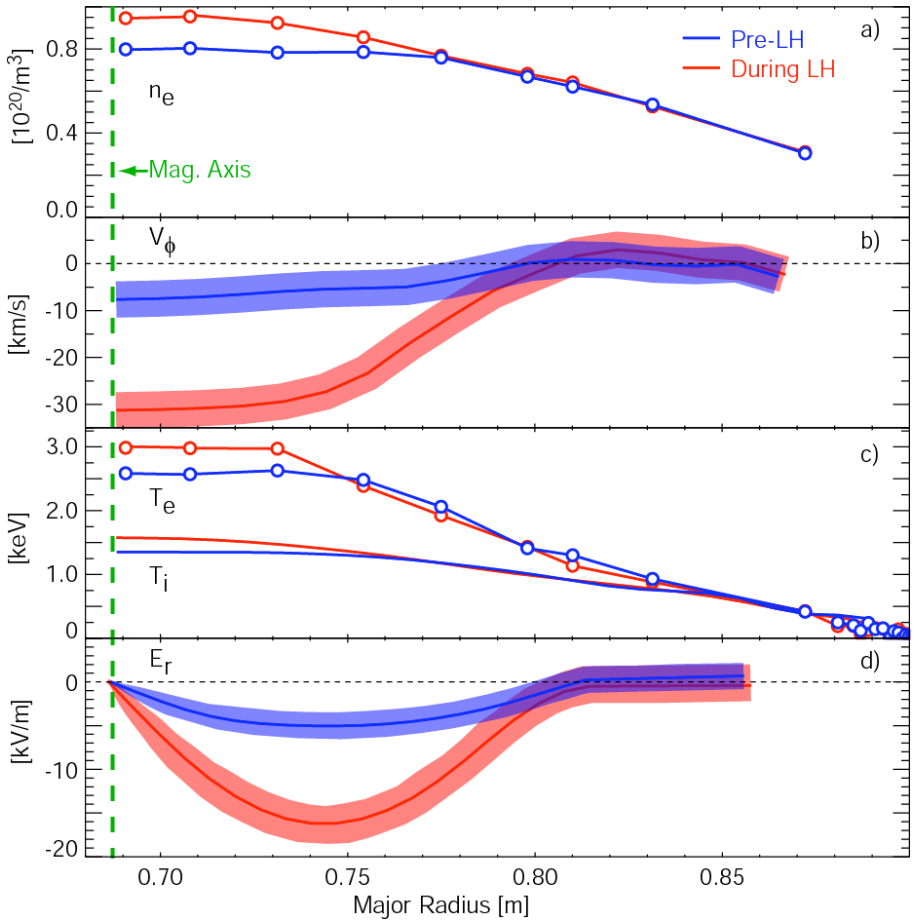

Fig. 3.9. Profiles of a) electron density, b) toroidal velocity, c) electron and ion temperature and d) inferred radial electric field before and during the application of LHCD. C-Mod.

A possible explanation of this negative charging of the core is a resonant trapped electron pinch. This pinch is the result of the canonical angular momentum absorbed by resonant trapped electrons while interacting with lower hybrid waves. Since the trapped resonant particles cannot on average carry toroidal mechanical angular momentum, the added momentum can only be realized by a change in the electron vector potential, and so they are forced to drift radially inwards. This mechanism can be thought of as a "Ware pinch"-like effect operating on resonant trapped electrons. The Ware pinch is automatically ambipolar because it is based on the $E \times B$ drift associated with the toroidal electric field and the poloidal magnetic field. In the LHCD case, however, the resonant electrons experience a larger electric field than the ions and therefore a faster drift. This in turn, gives rise to a non-ambipolar inward radial drift of electrons, and therefore negative charging of the core. A pinch of resonant electrons is consistent with the observation that no change in radial electric field is seen when LHCD is applied in the counter-current direction. In this situation, virtually no fast electrons are produced

because the LHCD is countered by the opposing Ohmic electric field. With no fast electrons there can be no fast electron pinch.

Regardless of the details of the electron pinch mechanism, as the plasma charges up negatively, the radial electric field is modified so as to oppose this charge separation. This negative increment in the radial electric in turn drives counter-current toroidal rotation via radial pressure balance. In steady state, the negative charging due to the electron pinch is balanced by a return current produced by the altered radial electric field.

3.3. INTRINSIC ROTATION SCALING

The multi-machine database for intrinsic rotation [6] indicates that there is a common physics basis to the effect. In engineering parameters this database was first organized by Rice and co-workers by $V_\phi \sim W/Ip$, which is typically referred to as Rice scaling [2]. An experimental effort continues to probe this scaling further, and to seek to find a representation of the scaling in terms of the dimensionless parameters of the plasma (see Sec. 3.4)

There are new data points from the ASDEX Upgrade and JET tokamaks which fall in with the multi-machine intrinsic rotation scaling of M_A vs β_N. Here, M_A is the intrinsic toroidal velocity scaled to the Alfvén velocity, and β_N is the normalized plasma beta, a measure of the stored energy in the plasma. The scaling with β_N is not as strong as seen on other devices.

Additional details will appear in the publication cited in Appendix B.4.

3.4. L-MODE INTRINSIC ROTATION IN C-MOD, C-MOD – TCV SIMILARITY EXPERIMENTS

One method to further the understanding of intrinsic rotation is to perform joint experiments on different tokamaks, to identify mechanisms that are universal from those that could potentially be specific to one machine. L-mode discharges, and especially limited L-mode discharges (in contrast to poloidally diverted discharges) exhibit a wider variety of toroidal rotation profiles than seen in H-mode. Understanding such variety can help to find dominant causal mechanisms, whether classical or due to a turbulent drive.

Rotation inversion, the abrupt change in rotation direction, has been observed in plasmas in the TCV tokamak [7] following very small changes in the electron density [8], when q is near 3. A C-Mod – TCV similarity experiment has been performed in order to try to reproduce these results. Shown in Fig. 3.10 are the time histories of three C-Mod limited discharges which demonstrate abrupt rotation inversions, which occur near $q = 3$. In these cases the electron density doesn't appear to be playing the same role as in TCV, but the inversions seem to be similar. Further analysis and experiments are planned.

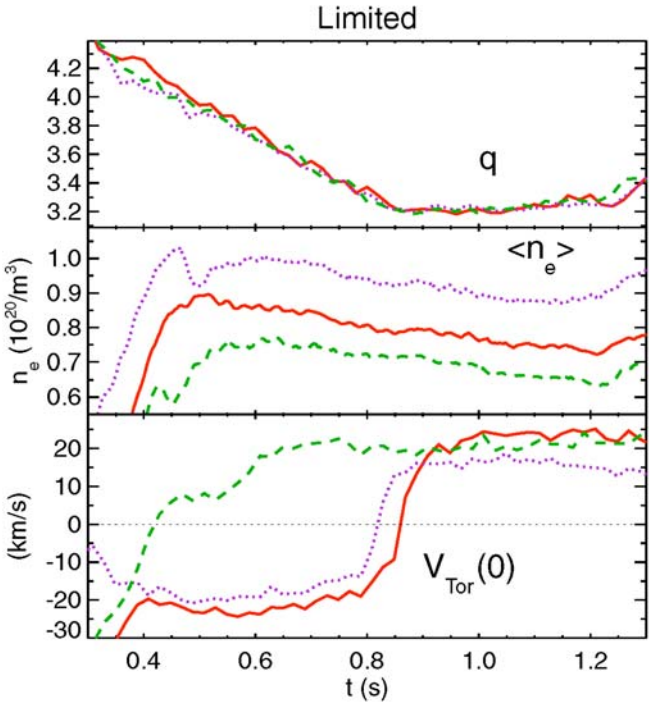

Fig. 3.10. Toroidal rotation velocity time histories (bottom) for three discharges with rotation inversions: a) q limited, b) density, and c) toroidal velocity. C-Mod.

3.5. INTRINSIC ROTATION WITH NEAR-BALANCED NEUTRAL BEAM INJECTION IN DIII-D

3.5.1. Introduction

Intrinsic rotation in the tokamak is the experimentally discovered result [2-9] that the plasma has a nonzero toroidal velocity even with no auxiliary injected momentum, usually due to NBI torque. Toroidal rotation has also been determined to be important for issues of stability and confinement, and as such it is recognized to be important for ITER operation. The planned NBI torque for ITER will be relatively small [10] compared with present experimental capabilities and thus it will be the intrinsic rotation that will most likely dominate the toroidal velocity in ITER. Past experiments in DIII-D clearly indicate that the NBI torque drive is additive on some intrinsic base [9].

A rather comprehensive database of intrinsic rotation results has been assembled from a number of tokamaks throughout the world [6]. In general the intrinsic toroidal velocity, V_ϕ, follows the Rice scaling, $V_\phi \sim W/Ip$ [2,11,12]. Here, W is the stored energy in the plasma, and I_p is the magnitude of the toroidal plasma current. An intrinsic velocity driven by "heating", the W dependence, has become recognized by theories that attempt to explain it [13]. This construction of the scaling law is in terms of the so-called engineering parameters, stored energy and total current, equivalent to the extrinsic variables of thermodynamics that simply get bigger as the system gets bigger. However,

theoretically one expects the thermodynamic intrinsic variables to be behind the generation of an intrinsic flow, those that are locally determined within the plasma, whether due to turbulence or classical collisional effects. This is empirically reflected in the fact that the proportionality in the Rice scaling law is smaller in DIII-D than C-Mod, with DIII-D about 2.5 times larger in linear dimension than C-Mod.

In plasma physics a scaling law stated in intrinsic variables is cast in terms of the dimensionless variables that describe the plasma, known as dimensional similarity in fluid dynamics. The Rice scaling has also been fit in the form $M_{th} \sim \beta_N$, and also $M_A \sim \beta_N$ [6], where the database does not clearly allow a selection of one as a better scaling law. Here, dimensionless local velocities are defined by scaling V_ϕ to the ion thermal velocity for M_{th}, and to the Alfvén velocity for M_A, $M_{th} \equiv V_\phi / \overline{V_i}$, $M_A \equiv V_\phi / V_A$, with $\overline{V_i} \equiv \sqrt{T_i}/M$, $V_A \equiv B/\sqrt{\mu_0 n_i M}$, with T_i the ion temperature, B the magnetic field strength, n_i the ion density, M the ion mass. The value of W/Ip is directly proportional to β_N at fixed B, so it is not too surprising that the Rice scaling can be cast in this form.

The pre-2008 data that make up this empirical scaling are limited to β_N below about 1.3 since the H-mode discharges in this set are invariably achieved with rf heating and these auxiliary systems have less power available than the dominant NBI heating systems. The target β_N value for an initial inductive scenario in ITER [10], is approximately 2. Clearly, it is important to extend the database to ITER-relevant values of β_N.

The balanced NBI capability provides DIII-D with the capability to demonstrate intrinsic rotation in higher β_N H-mode conditions and reach ITER-relevant values. Past DIII-D experiments have clearly shown the existence of an intrinsic co-Ip velocity that exists with the global NBI torque near zero [14]. However, making such a measurement with an effective accuracy that allows it to be confidently placed into a scaling requires careful planning and analysis. This is because the torque from a co-Ip and an equivalent counter-Ip injected neutral beam will never cancel locally everywhere within the plasma. The physics issue that precludes perfect cancellation is that upon deposition within the plasma, on the outboard side of the magnetic axis, the drift of a co-Ip fast NBI ion carries it toward the magnetic axis, while that for a counter-Ip fast NBI ion carries it away from the magnetic axis. The drift excursions are opposite for those fast ions born inboard of the magnetic axis. The plasma density and temperature profiles determine the fast ion birth profile so that the resultant torque imbalance will depend upon plasma conditions.

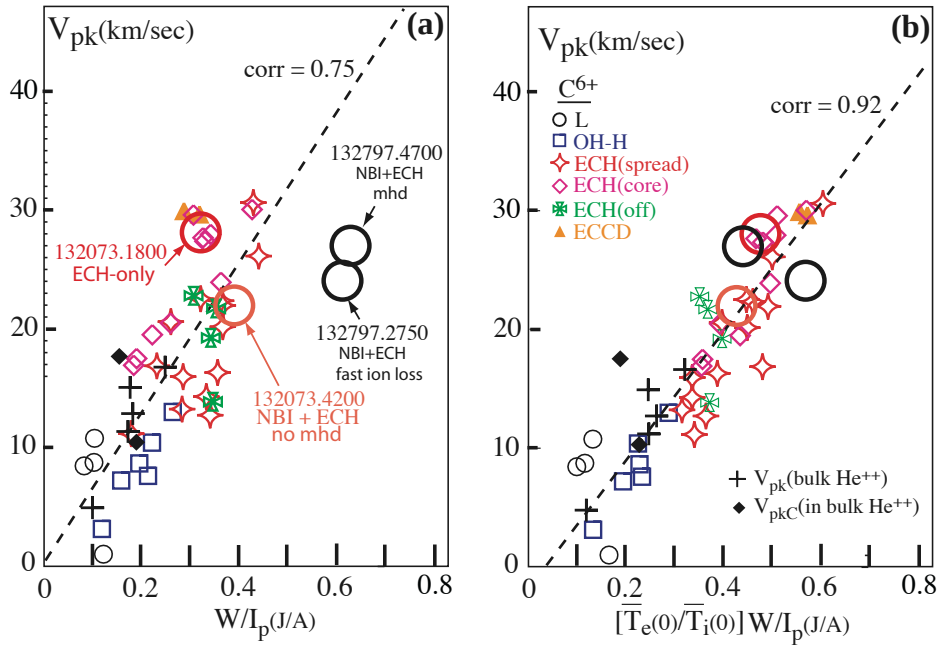

Fig. 3.11. New datapoints placed upon the former V_{pk} scaling of intrinsic velocity in DIII-D. The large red circles are for ECH-only, with similar conditions to the former database, and NBI + ECH. These time points show no indication of added anomalous transport. The large black circles are from two time slices in a discharge with added anomalous transport. (a) vs the standard Rice scaling parameter W/I_p and (b) vs $W/I_p \times [T_e/T_i]$ core.

Nevertheless, we have found that we can disentangle the intrinsic rotation from careful experiments with near-balanced NBI in 2008 in DIII-D, and have reached β_N values above 2, our goal. We have many discharges that require in depth analyses and which we will use to extend the database. Here, we give results from some discharges analyzed to date. We believe that the Rice scaling continues to higher β_N.

3.5.2. Extending the Intrinsic Rotation Database to Higher β_N

First we test our methodology by measuring where our measurements fall in the existing DIII-D intrinsic rotation database in a purely ECH H-mode case, with no significant NBI momentum, and then with a moderate amount of NBI added with near zero net toroidal torque.

In Fig. 3.11 we show where this intrinsic ECH H-mode velocity point falls relative to the DIII-D Rice scaling database for ECH H-modes from experiments in 2002 and 2004 [9,15,16]. In DIII-D we found that the basic Rice scaling organized our data if we focused upon the spatial location $\rho \cong 0.8$. Inside this region the intrinsic velocity depends upon the details of the ECH deposition location. The smaller symbols in Fig. 3.11(a) are from this past dataset, with different symbols representing different ECH deposition conditions. This is the basic, original Rice parameterization, V_ϕ versus W/Ip. Here, V_{pk} refers to $V_\phi(\rho \cong 0.8)$. The large open circle (orange) with label 132073.1800 with ECH

only and a value of $\beta_N = 1$. This point falls within the former set, even though the detailed shape in this LSN plasma is a bit different due to the installation of the lower divertor shelf in DIII-D between 2004 and 2006. The correlation in the former dataset shown in Fig. 3.11(b) was an extension to the Rice scaling that we found gave a tighter fit. Here, we multiply W/Ip by $\overline{T}_e(0)/\overline{T}_i(0)$, an average of the core electron temperature, T_e, divided by an average of the core T_i over the range $0 \le \rho \le 0.3$. Again, this latest ECH H-mode point falls well in with the former data.

With the addition of balanced NBI at a power level near that of the ECH power the value of β_N rises to 1.2. This point with ECH and balanced NBI is also shown on the graphs in Fig. 3.11, with the label 132073.4200, and again fits quite well into the former database, in both correlations shown. We conclude that additive NBI at this level well maintains the Rice scaling for intrinsic toroidal velocity.

One important point for this particular discharge is that the total neutron rate computed with the Monte-Carlo TRANSP analysis code matches very well with the measured value. This is not the case when we go to higher balanced NBI power. Magnetohydrodynamic instabilities and fast ion instabilities reduce the fast ion confinement time and presumably also the toroidal momentum confinement time, leading to a degradation in the intrinsic toroidal velocity, as we see with increased β_N.

Two timeslices are picked in a shot with higher NBI power with β_N values of 1.9 and 2.0, respectively, the latter having ECH added to the NBI power. These values of V_{pk} are also added to the database results in Fig. 3.11. These points fall below the fitted line from past analysis. When added to the plot in Fig 3.11(b) both tend to fall well into the former fit. In both timeslices the core T_i exceeds the core T_e, tending to move the horizontal axis value closer to the origin in Fig. 3.11(b), and hence closer to the fitted line. With high power NBI we usually find that $T_i > T_e$, so this is not unusual for high power NBI alone. However, with high power ECH H-modes the core $T_e > T_i$ and this is the situation for a large portion of the original database shown in Fig. 3.11. In contrast, in this mixed situation with high power ECH added to high power NBI later in the shot we still have a significant $T_i > T_e$ in the core. Although T_e increases with ECH, T_i increases more due to a density reduction with added ECH in the presence of strong ion heating from NBI. Since it is likely that the intrinsic rotation is the result of some boundary condition in conjunction with a turbulent momentum pinch, the strength of the pinch could depend upon T_e/T_i in determining the details of the resultant turbulence.

We will continue to examine the database acquired in 2008 for a quantitative way to account for the reduction with momentum confinement experienced with higher β_N. At this time we hypothesize that the Rice scaling continues to hold at the ITER relevant β_N values, apart from the reduction in confinement that would be absent in the absence of MHD activity or fast ion instabilities.

4. MOMENTUM TRANSPORT

4.1. SUMMARY

Perturbative techniques have been used to develop a more comprehensive picture of momentum transport that can be determined through steady-state analysis, allowing a more direct connection to theory. The rapid change in torque locally and the plasma response to these changes can be modelled and used to decouple the diffusive part of the momentum flux, χ_ϕ, from the convective portion, V_{pinch}. Torque perturbations that were used include neutral beam pulses, braking pulses from applied magnetic fields and rapid shape changes. These experiments have shown that the description of momentum transport using only an effective diffusivity (i.e., convective terms assumed to be zero) is inadequate. The more comprehensive analysis indicates significant momentum pinch velocities on both DIII-D and NSTX, with values up to 40 m/s on both devices. This can impact the magnitude of the χ_ϕ by factors of several. This result is robust and independent of aspect ratio. The source of the momentum transport (e.g., pinch velocity, V_{pinch}) appears to be tied to low-k turbulence, which is a conclusion based on comparisons between experimentally inferred and theoretically predicted values of the momentum pinch velocity. This result is also robust and independent of aspect ratio, as well as being independent of the enhancement of ion thermal diffusivity over neoclassical for NSTX. These results suggest that momentum flux (both χ_ϕ and V_{pinch}) predicted from low-k turbulence theory could be used as reasonable estimates for predicting rotation in future devices such as ITER. A challenge will be to determine these values quantitatively from theory.

Additional details will appear in the publications cited in Appendix B.5,6,7.

4.2. DIFFUSIVITY AND PINCH IN NSTX (MAGNETIC BRAKING SOURCES)

Momentum diffusivity values determined from steady-state analysis show that there is a general correlation between χ_ϕ and χ_i in the outer region of the plasma $(r/a > 0.5)$, but with $\chi_i >> \chi_\phi$, but not in the very core $(r/a < 0.5)$. Because of the coupling between χ_i and χ_ϕ in the outer region of the plasma, where χ_i can often be close to neoclassical, it is natural to explore whether χ_ϕ is also controlled by neoclassical processes. GTC-NEO has been used to address this, with the results for H-modes shown in Fig. 4.1. Plotted in this figure are the experimentally inferred χ_i and χ_ϕ (solid blue and red lines respectively) along with the values determined from GTC-NEO (dashed blue and red lines). For this H-mode discharge, it can be seen that while the experimentally inferred χ_i is essentially at the neoclassical level across the plasma, $\chi_\phi >> \chi_{\phi,neo}$, which is

essentially zero. This result is robust, even when $\chi_i/\chi_{i,neo} > 1$, as in high density L-mode plasmas. This result indicates, therefore, that the primary driver for the momentum transport must be something other than neoclassical processes.

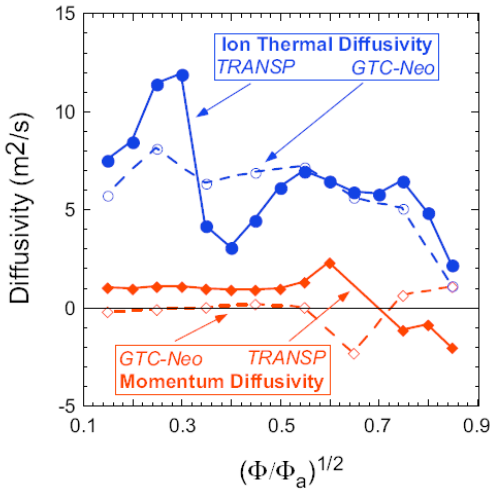

Fig. 4.1. Experimentally inferred values of χ_i and χ_ϕ compared to the neoclassical values as computed by GTC-NEO. NSTX

To develop a fuller picture of momentum transport, both the momentum diffusivity and any possible momentum pinch must be determined. To accomplish this, torque perturbations were applied using either 200 ms neutral beam pulses of approximately 2 MW (in addition to steady 2 MW injection), which changed rotation primarily in the core, or 50 ms pulses of $n = 3$ braking fields, which changed the rotation primarily in the outer (gradient) region. The results for a case in the outer portion of the plasma, is shown in Fig. 4.2. The momentum diffusivity is shown for a case where V_{pinch} is assumed to be zero, and for the case with a finite V_{pinch} assumption in solving the above equation. It can be seen that the χ_ϕ with non-zero V_{pinch} can be several times larger than that when V_{pinch} is assumed to be zero. The inward pinch can be significant (bottom panel), in this case with a value of up to 20 m/s in the region from $r/a = 0.6$ to 0.8, and reaching up to 40 m/s in other cases. I_p and B_T scans revealed a decrease in χ_ϕ with B_T in the outer region of the plasma, but little dependence of χ_ϕ or V_{pinch} with plasma current. No dependences were observed in the core region.

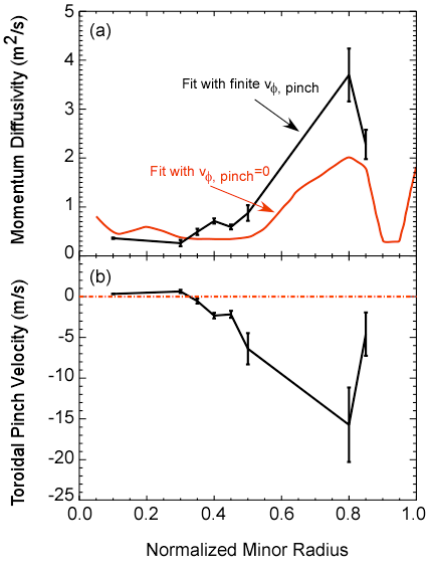

Fig. 4.2. (a) momentum diffusivity and (b) pinch velocity inferred using $n = 3$ magnetic braking. The inferred diffusivity assuming $V_{pinch} = 0$ is shown in red. NSTX.

There are theories suggesting that the source of the momentum pinch is low-k turbulence in the plasma [17-20]. Two theories [17,18] find that $V_{pinch} \sim \chi_\phi / R$, although Peeters [17] claims an additional dependence on the density gradient scale length, L_n. A comparison of V_{pinch} as computed by these two theories to the experimentally inferred values for the outer region of the plasma is shown in Fig. 4.3. The red points in the figure show the V_{pinch} computed by the Hahm theory [18], while the blue points show those computed with the Peeters theory [17]. In general, both theories indicate reasonable agreement with the inferred values, although Peeters theory, while introducing more scatter, appears to fit better especially for larger V_{pinch}. The better fit by the Peeters theory is due to the presence of the L_n term, especially at the lowest L_n where the experimentally inferred V_{pinch} is largest. In the inner region, the comparison between the inferred pinch velocities and those calculated by either theory was poor, for all L_n. This result is also consistent with linear gyrokinetic calculations indicating that ITG/TEM modes are unstable in the outer region, but stable in the core in these plasmas.

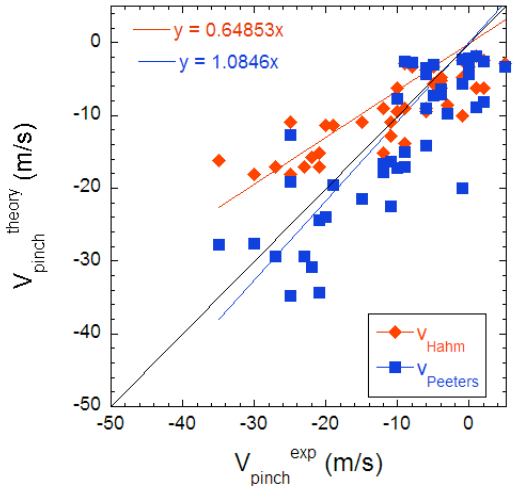

Fig. 4.3. V_{pinch} as computed by the Hahm (red) and Peeters (blue) theories vs experimentally inferred values. NSTX.

4.3. DIFFUSIVITY AND PINCH IN DIII-D WITH MODULATED NEUTRAL BEAM INJECTION

Experiments on DIII-D have made use of the capability to vary the torque at constant power to investigate the role of non-diffusive transport. In particular, perturbative studies of the rotation using combinations of co and counter neutral beams have revealed the existence of a momentum pinch in DIII-D H-mode plasmas. By modeling the evolution of the viscous angular momentum flux following a perturbation to the rotation, $\Gamma_\phi \propto -\left(\chi_\phi \partial V_\phi / \partial r - V_\phi V_{pinch}\right)$, where χ_ϕ is the momentum diffusivity and V_{pinch} represent a pinch of momentum, then provided that toroidal velocity V_ϕ and its spatial gradient dV_ϕ / dr, evolve independently, the diffusive and convective components can be decoupled. The inferred inward momentum pinch velocity from such an analysis shows qualitative similarity to theoretical predictions resulting from consideration of low-k turbulence, in particular, showing a radial dependence proportional to the momentum diffusivity, as is seen in Fig. 4.4. Relatively good agreement is observed across the profile, although the notable discrepancy outside of $\rho \sim 0.8$ still needs to be understood. In the presence of an inward pinch of momentum, the inferred χ_ϕ is generally larger than from a steady-state analysis that treats the transport purely in terms of an effective diffusivity. It is therefore unlikely that an effective χ_ϕ will be satisfactory for prediction of the rotation profile.

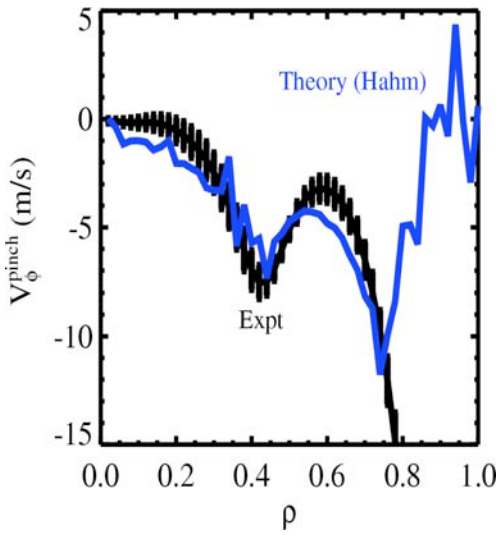

Fig. 4.4. Experimentally determined pinch velocity from perturbation experiment (black) compared with theory of Hahm (blue). DIII-D.

4.4. RAPID SHAPE CHANGE IN C-MOD

It has been demonstrated that the Ohmic L-mode toroidal rotation velocity depends very sensitively on the balance between upper and lower null under certain operating conditions. In particular, discharges with the unfavorable drift direction exhibit a stronger counter-current rotation than those with favorable drift, and this is related to the H-mode power threshold. The X-point can be switched dynamically during a single discharge and the core rotation velocity has been observed to respond in kind, as is shown in Fig. 4.5.

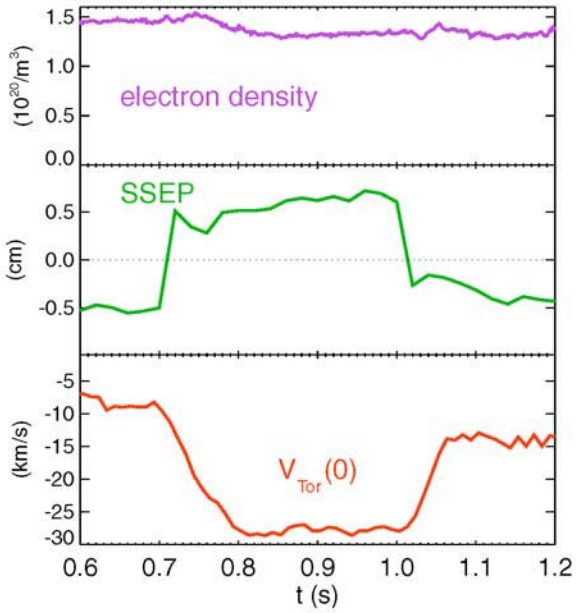

Fig. 4.5. SSEP (middle) and the core toroidal rotation velocity (bottom) for a LSN discharge which was changed to upper null at 0.7 s and back at 1.0 s. C-Mod.

Since the rotation velocity perturbation in these cases must be occurring at the plasma edge (only the edge magnetic field structure was changed), this technique allows determination of the momentum transport coefficients through observations of the core rotation velocity profile evolution response.

Shown in Fig. 4.6 are the toroidal rotation velocity time histories along several chords for a discharge with a rapid SSEP change. SSEP measures the up/down bias of the plasma symmetry relative to the midplane. The momentum confinement time in this case was about 40 ms, in agreement with earlier indirect measurements. This technique will allow for a characterization of momentum transport parameter dependences in L-mode plasmas.

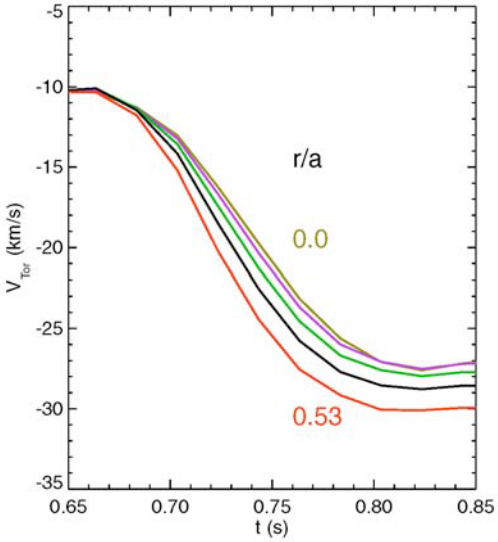

Fig. 4.6. Toroidal rotation velocity evolution along several chords following a rapid SSEP change. C-Mod.

4.5. INTRINSIC ROTATION PROFILE EVOLUTION

4.5.1. Overview

The new spectrometer system on C-Mod provides detailed velocity profile measurements. This has been used to further verify former results in C-Mod [21] that the intrinsic momentum source appears to originate at the plasma edge and propagate inward, as can be described by a model for toroidal momentum flux that has a diffusive and a pinch term [21].

Most experiments that have measured an anomalous pinch term utilize external torque modulation with a neutral beam source. It is important to establish, and measure both the pinch and diffusivity terms in the case of pure intrinsic velocity, as done in these C-Mod experiments.

4.5.2. Experimental Results

The installation of the new imaging x-ray spectrometer on C-Mod [22] allows for velocity profile evolution measurements greatly improving upon the results from the previous three chord system. Shown in Fig. 4.7 are the rotation time histories for several different chords for an H-mode plasma. The toroidal rotation velocity propagates in from the outside following the H-mode transition, indicating an edge source for the co-current rotation in H-mode.

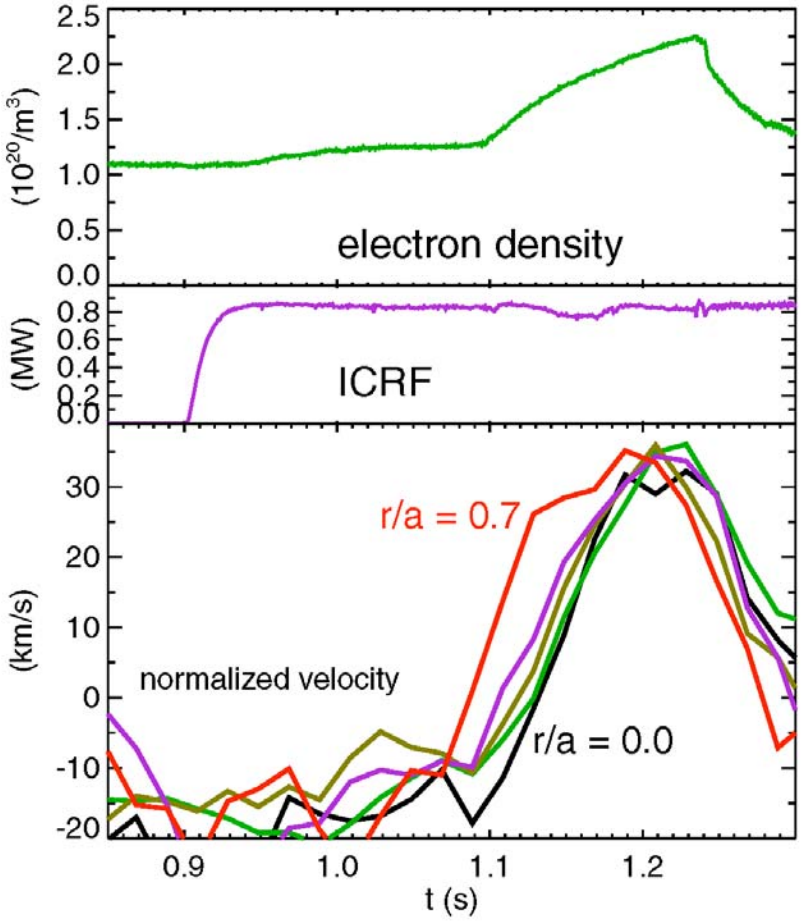

Fig. 4.7. Toroidal rotation velocity time histories for several different chords for an H-mode plasma. C-Mod.

The new system also reveals detailed profile shapes. Shown in Fig. 4.8 are toroidal rotation velocity profiles in L-mode, in an ELM-free H-mode, and in the transition time between these states. During the fully developed H-mode (shown in red), the velocity profile is centrally peaked, indicating the presence of an inward momentum pinch. There have recently been several theories [17,18] predicting the magnitude of the inward pinch velocity, and the new profile measurement capabilities will allow detailed comparison with theory, similar to ongoing work at DIII-D.

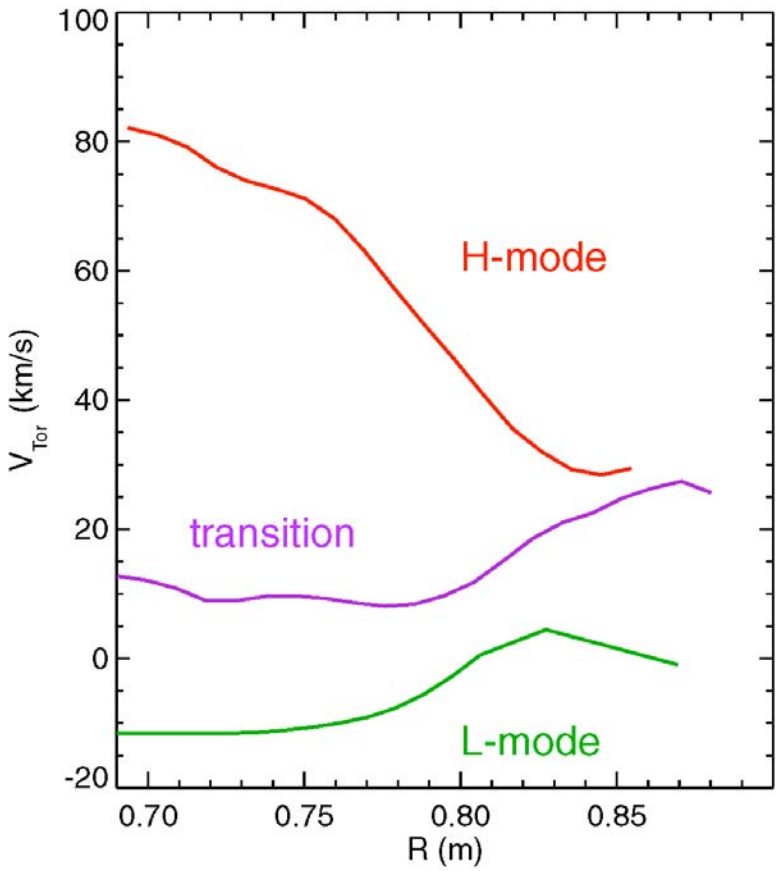

Fig. 4.8. Toroidal rotation velocity profiles for L-mode (green), just after the H-mode transition (purple) and in a fully developed ELM-free H-mode (red). C-Mod.

5. MOMENTUM SINKS

5.1. SUMMARY

Nonresonant magnetic perturbations apply a drag to rapidly rotating plasma discharges. This effect has been verified in past experiments in NSTX [23], and found to agree with the relevant theory of so-called Neoclassical Toroidal Viscosity (NTV) [24]. NSTX experiments this year have expanded the study of NTV by using n=2 applied fields, to compare with former experiments that used n=3 perturbations, where n is the toroidal mode number.

In the lower rotation limit, NTV theory predicts an offset, nonzero steady state velocity. DIII-D experiments this year identified this offset toroidal rotation, which is in the counter-Ip direction. The agreement with theory is not far off, but there is an issue regarding the theoretical predictions relative to the collisionality of the plasma. The theory is done in two different limits, one the extreme with very low collision frequency, and the other with a somewhat high collision frequency [25]. To match the offset velocity DIII-D uses a multiplier between these two collisional limits.

The importance of collisionality in NTV theory has been tested experimentally this year in NSTX by varying the ion temperature, T_i. The results are consistent with theory in that higher T_i produces greater NTV damping of rotation. Other NSTX experiments have shown that correcting nonresonant error fields leads to an enhanced operating space for the plasma.

Resonant magnetic perturbations have a structure that matches the helicity of a surface within the plasma, and are known to cause very strong rotation damping, and can result in the dangerous locking phenomenon wherein the plasma ceases to rotate. Locked plasmas are susceptible to disruption. DIII-D experiments found that by considering the response of the plasma to a resonant magnetic perturbation that the results in two very different plasma limits, one low energy and one high energy, can be unified.

5.2. NEOCLASSICAL TOROIDAL VELOCITY IN DIII-D

5.2.1. Introduction

Nonresonant magnetic error fields produce a toroidal torque on the plasma. The theory that describes this effect is given by computations of the Neoclassical Toroidal Viscosity (NTV) [24]. One potentially positive result from this effect is the prediction of an offset toroidal velocity in the direction opposite to that of the plasma current, counter-Ip. Thus, NTV might be useful in generating a nonzero toroidal rotation in burning plasmas, such as ITER. Experiments in DIII-D have observed such an offset rotation with

the application of nonresonant n=3 magnetic perturbations, where n is the toroidal mode number.

Additional details will appear in the publication cited in Appendix B.8.

Suppression of ELMs has been accomplished in DIII-D with the use of resonant magnetic perturbations, RMP. The dominant resonance is in the edge of the plasma where the ELM instability appears to be generated. However, these n = 3 RMPs also produce nonresonant perturbations which should be described by NTV theory. ITER is considering added RMP coils for ELM suppression. It is an urgent issue to understand if the NTV effects from these RMP coils will be beneficial or deleterious in ITER.

5.2.2. Experimental Evidence of Offset Rotation due to NTV in DIII-D

Recent DIII-D experiments have shown the first evidence of a nonresonant braking torque that is proportional to $(\Omega - \Omega_0)$, where Ω_0 is an "offset" rotation in the counter-Ip direction. The existence of such an offset rotation is predicted by neoclassical theory of toroidal flow [24]. DIII-D data showing the existence of this offset rotation are shown in Fig. 5.1.

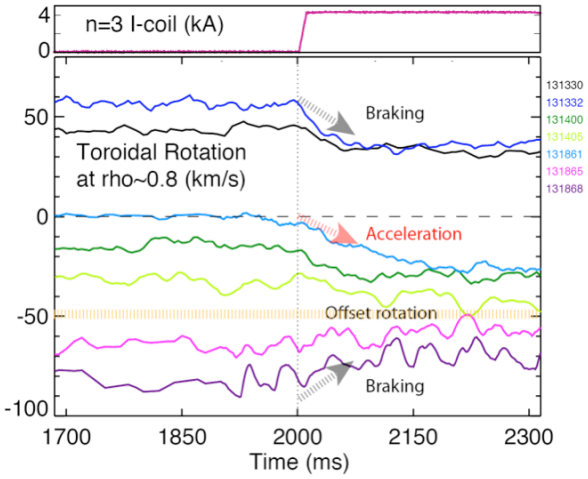

Fig. 5.1. Effect of large nonresonant n=3 fields applied by the I-coil on DIII-D plasmas depends on the initial toroidal rotation. Co-Ip rotation is slowed down. Slow counter-Ip rotation is accelerated. Fast counter-Ip rotation is slowed down.

When a large n=3 field is applied to an already co-rotating plasma, a spin-down is observed. When the n=3 field is applied to a near stationary (near balanced NBI) or slowly counter-rotating plasma, a strong acceleration of the plasma rotation in the counter-Ip direction is observed. The application of the n=3 field also leads to an increase in the energy confinement. The rotation acceleration happens at all radii, largest at $\rho \sim 0.7$. When the n=3 field is applied to a plasma with an already fast counter-rotation, again a spin-down is observed. What is measured is the carbon ion rotation, which allows the determination of the species-independent toroidal rotation driven by the radial electric

field, ω_E. When the n=3 field is applied to a near stationary plasma, the ω_E rate is observed to increase (in the counter direction) as well as the carbon rotation, consistent with the confinement effect. Note that the ω_E rate also is the rotation that is important for stability of the Neoclassical Tearing Modes [26] and RWM [27].

The offset rotation is of the order of the ion diamagnetic drift rotation. Theory predicts

$$\Omega_0 \sim k_c \frac{R_0 q \nabla T_i}{Z_i e r B_0 R} \quad ,$$

with $k_c = 3.5$ for the $1/\nu$ collisionality regime, and $k_c = 0.9$ for the lower collisionality ν regime [25]. For DIII-D, the offset rotation is obtained using $k_c = 1.9$. Using the same $k_c = 1.9$ for ITER Scenario 2 plasmas, the predicted offset rotation is shown in Fig. 5.2. It is the same in magnitude as the unperturbed rotation (rotation without nonaxisymmetric fields). The equilibrium rotation of ITER will depend on the relative magnitude of the nonresonant field torque to the neutral beam torque, and other sources of torque (e.g. intrinsic rotation). If the nonresonant field torque dominates, the plasma will rotate close to the offset rotation.

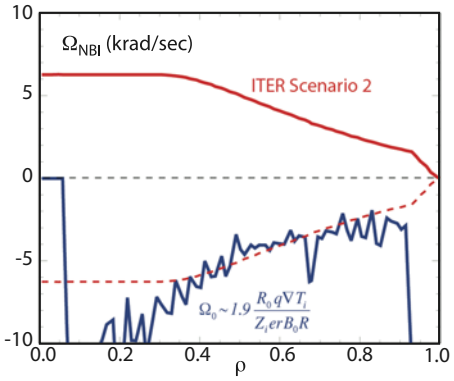

Fig. 5.2. Offset rotation (blue) predicted for ITER Scenario 2 plasmas. Predicted NBI-driven rotation (red). (The dotted red line is the red inverted for comparison.) DIII-D.

5.2.3. Physics Understanding

Various processes contribute to toroidal viscosity enhancement due to the application of nonaxisymmetric magnetic fields: untrapped-particle ripple drag, trapped-particle ripple drag, and trapped-particle radial banana-drift. It is believed that in fusion plasmas, the main effect comes from trapped-particle radial banana-drifts. This effect depends on the ion collisionality ν_i relative to the toroidal flow driven by the electric field, ω_E. The calculations by Becoulet [28] shown in Fig. 5.3 are estimates of the neoclassical toroidal flow damping due to trapped-particle radial banana-drifts in the $1/\nu$ collisionality regime, where $\omega_E < \nu_i / \varepsilon$.

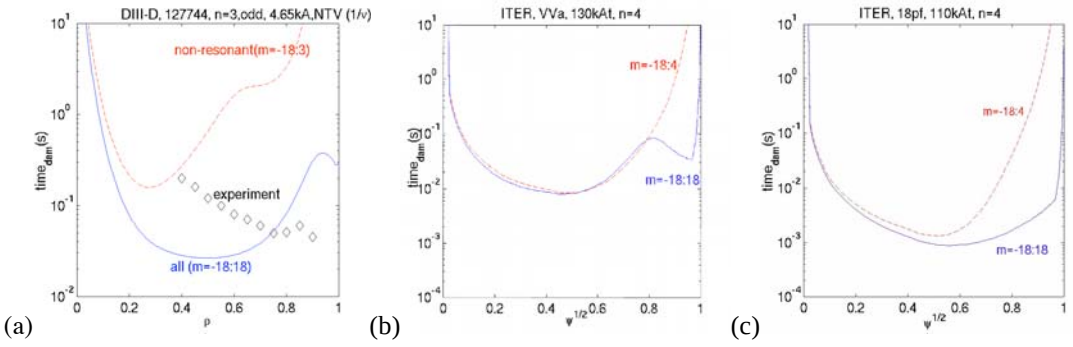

Fig. 5.3. Predictions of the damping times due to neoclassical toroidal torques ($1/\nu$ collisionality regime) from nonresonant magnetic fields (range of poloidal harmonics used in the computations is indicated next to the resulting curve). (a) Predictions for DIII-D discharge #127744 with n=3 I-coil field, compared to measurements. (b, c) Predictions for ITER Scenario 2 discharges with n=4 fields from two different RMP coil configurations. (b) four rows, (c) one row. Magnetic fields calculated in vacuum. Broad n and m spectra are used.

One caveat is that vacuum magnetic field calculations are used, i.e. the plasma response to the I-coil field is neglected. In DIII-D, we have measured the plasma response to the n=3 field, and we find that it is relatively large at the magnetic sensors. The exact magnitude of the internal plasma response has not been calculated yet, but simple considerations extrapolate to a field that is at least of similar magnitude to the vacuum field. Therefore, neglecting the plasma response could cause an error of more than a factor of two (torque is proportional to field squared).

Another important caveat is that the assumption that the DIII-D plasma is in the $1/\nu$ collisionality regime is not correct. Most of the plasma is in the low collisionality ν regime, for which $\omega_E > \nu_i/\varepsilon$. In this regime the nonresonant field torque is expected to be smaller.

The calculations by Becoulet (shown in Fig. 5.3) represent the state of the art for modeling of the neoclassical torque from nonresonant fields on DIII-D and ITER. However, the relatively good agreement with the experimental measurements in DIII-D may be resulting from the fortuitous compensation of effects of various approximations. The $1/\nu$ regime calculations may be overestimating the torque from a given field, by as much as one order of magnitude. On the other hand, neglecting the plasma response leads to underestimating the magnitude of the perturbed field, therefore underestimating the torque by as much as one order of magnitude.

If the ITER plasmas are in the same viscosity regime as the DIII-D plasmas, and if the plasma response in ITER behaves similarly to DIII-D, then the predictions can still be meaningful. Indeed, both ν_i and ω_E in ITER are expected to be significantly lower than in DIII-D, therefore their ratio may remain similar to the DIII-D case used to benchmark the model.

5.2.4. Recommendation

Our physics understanding of the effects of nonresonant fields on the toroidal rotation of a fusion-grade plasma is still developing. Complete modeling of the neoclassical theory of toroidal flow is not yet possible, and benchmarking with experiments has only recently started. Surprising and important features of the theory are just now being observed in the experiment for the first time.

It appears likely that the nonresonant field torque from one of the proposed RMP coil sets for ITER would be larger than the ITER NBI torque. However, at present it is unclear whether such a large nonresonant field torque would have a negative or positive impact on the performance of ITER, because

1. If the neoclassical offset rotation in ITER is negligible, the nonresonant field torque from any of the proposed RMP coil sets for ITER would likely damp the rotation to zero, with negative effects on stability and confinement.
2. If the neoclassical offset rotation in ITER is large (and theory suggests it could be), the RMP coil set causing the larger nonresonant field torque would be more likely to force rotation at the neoclassical offset value, with positive effects on stability and confinement.

On the basis of which coil set is most likely to produce the desired ELM suppression, the multi-row coil set has been recommended as preferable. It also has the advantage of a great deal of flexibility in the applied spectrum, which could be used to maximize or minimize the nonresonant field torque. At present, the uncertainties in all of the predictions for the nonresonant field torque and its effects are very large, due to the early stage of developing physics understanding. For these reasons, it is recommended that the coil set providing the maximum flexibility in the spectrum of the applied RMP field be chosen for ELM suppression in ITER.

5.3. NEOCLASSICAL TOROIDAL VELOCITY: NON-RESONANT MAGNETIC BRAKING: EVEN PARITY FIELDS AND COLLISIONALITY DEPENDENCE IN NSTX

5.3.1. Introduction

Physics understanding of non-axisymmetric field-induced plasma viscosity is important to future burning plasma devices including ITER, especially if magnetic ELM mitigation techniques will be used and in the compact toroidal facility (CTF) if rotation profile alteration is desired for global mode control. Non-resonant field application for toroidal rotation control is desired to minimize excitation of MHD modes. Braking torques due to odd parity applied fields has been quantitatively compared to neoclassical

toroidal viscosity theory in NSTX. [23] The non-resonant nature of the magnetic braking was recently studied using field configurations with dominantly even toroidal components. Recent experiments clearly demonstrate non-resonant braking using the n = 2 field configuration, which has a dominant n = 2 component, a significant n = 4 component (66% of the n = 2 amplitude), as well as smaller n = 8 and 10 components. The experimentally observed rotation damping profile is broader than that found for n = 3 fields, which is theoretically expected due to the broader field spectrum and reduced radial falloff of the n = 2 field.

A significant aspect of the NTV theory for ITER and an ST-CTF is the strong increase in NTV torque that occurs as the ion collisionality drops below the trapped particle bounce frequency, $\nu^* < 1$ (the torque scales as $1/\nu_i$ - the so-called "$1/\nu$" regime). In this ion collisionality regime, the non-ambipolar flux that leads to NTV is decreasingly perturbed by collisions, which increases the NTV torque. The dominant scaling of the theoretical NTV torque in this collision frequency regime (appropriate for present NSTX experiments) [23] has a strong dependence on the ion temperature, $\tau_{NTV} \sim \delta B^2 \varepsilon^{1.5} p_i / \nu_i \sim T_i^{5/2}$. While at sufficiently low collisionality the NTV torque is expected to saturate and then decrease (the torque scaling linearly with ν_i - the so-called "ν" regime), the collisionality at which the transition occurs, the magnitude of the NTV torque where saturation occurs, and whether or not a high NTV torque plateau vs. ν_i exists at low collisionality is an active area of research. Studying the scaling of τ_{NTV} vs T_i to as low a ν_i possible is important for future burning plasma devices such as ITER. In devices where plasma rotation control may be desired or required, such as in ST-CTF, it is important to verify $\tau_{NTV}(\nu_i)$, as it will determine the rotation profile in the presence of a non-resonant rotation control field.

Additional details will appear in the publication cited in Appendix B.9.

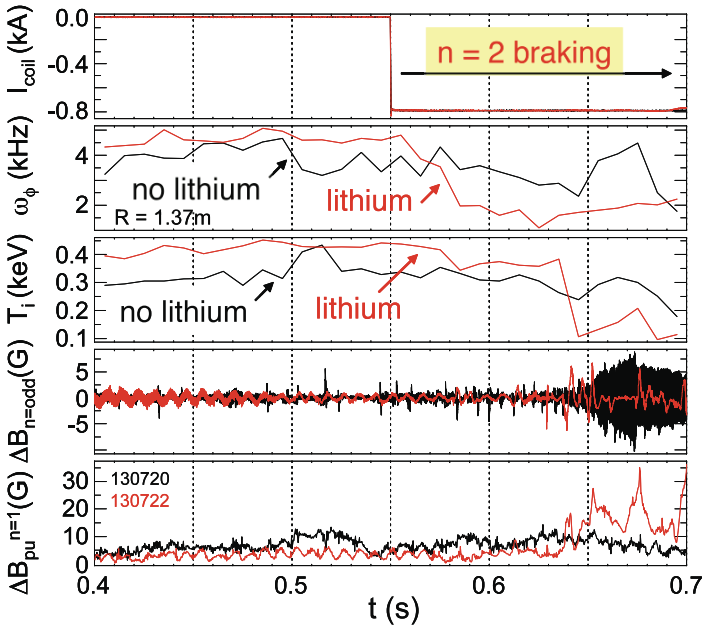

Fig. 5.4. Comparison of n=2 magnetic braking in plasmas with varied ion temperature. NSTX.

5.3.2. Recent Experiment

Recent NSTX experiments show that increased ion temperature increases the plasma rotation damping rate during non-resonant magnetic braking, consistent with a $T_i^{5/2}$ scaling of the NTV braking torque. The experiments utilized lithium evaporation to pre-condition portions of the divertor and plasma facing component carbon tiles. This technique [29] generates a significant increase in T_i in the region of peak n = 2 magnetic braking. Fig. III.3.1. compares two plasmas with equal magnitude of applied n = 2 braking currents, and with/without lithium wall preparation. The plasma without Li preparation displays a period of non-resonant n = 2 magnetic braking, which eventually transitions into a period of strong resonant braking caused by an n = 1 rotating MHD mode. In contrast, the plasma with Li preparation shows higher initial T_i (shown in the region of maximum change of ω_ϕ, R = 1.37 m) at the start of the magnetic braking pulse, with a ratio of T_i between the two shots of $T_i^{(\mathrm{Li})} / T_i^{(\mathrm{no\ Li})} = 1.324$. This yields a theoretically expected increase in τ_{NTV} of a factor of two in the plasma with higher T_i. This increase is consistent with the measured increase in the magnitude of $-d\omega_\phi / dt$ observed in the plasma.

5.4. ERROR FIELD AND NON-RESONANT MODE LOCKING EXPERIMENTS IN NSTX

In addition to the known resonant braking effects from n=1 error field, experiments in NSTX have shown the importance of correcting non-resonant error fields. This was demonstrated by a scan of the applied n=3 field amplitude and phase, illustrated in Fig.

5.5. The I_p and β_N waveforms illustrate that some discharges are sustained above the no-wall limit of $\beta_N \sim 3.8$ for many wall times, while other discharges suffer β_N collapses following the growth of Resistive Wall Modes (RWMs); these different discharge behaviors depend on the applied n=3 field.

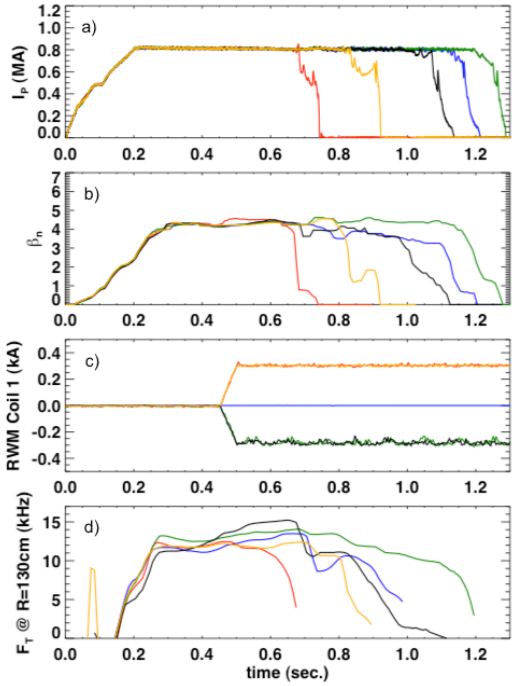

Fig. 5.5. The a) plasma current, b) β_N, c) representative RWM control coil current, and d) toroidal rotation frequency at R=130cm, as a function of time. NSTX.

The applied n=3 field is indicated in frame c) figure by the magnitude of the current in RWM control coil 1. For positive RWM control coil current in the orange and yellow traces, the plasma rotation is immediately slowed once the fields are applied, and the plasmas rapidly disrupt. The negative coil currents discharges shown in green and black lead to an increase in stabilizing plasma rotation and extension of the pulse length with the applied field (note that an n=1 rotation instability develops in the black case, leading to a somewhat premature termination of the discharge).

The dependence of plasma rotation and pulse length on the n=3 correction magnitude is shown more clearly in Fig. 5.6. The flat-top duration is shown as a function of RWM coil current in the top frame. While there is some scatter, there is a clear extension of pulse length with favorable sign of the n=3 field. The rotation at R=132 cm is shown in the bottom frame, as well as two mechanisms of determining the optimal correction current. The blue lines show a parabolic fit to the data and the predicted current for maximum rotation; the green lines show the optimum duration as predicted by two lines

on either side of the maximum. Both cases predict an optimal rotation in the vicinity of −300 A, consistent with the correction that leads to optimal pulse length.

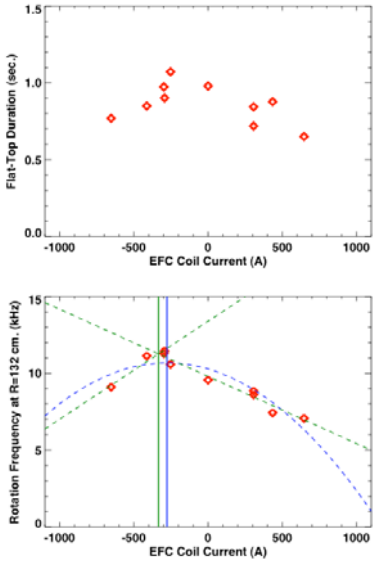

Fig 5.6. Plasma current flat-top duration and rotation at R=132cm (bottom), both as a function of the n=3 current in the EFC coils. The longest pulse-lengths occur for the correction current that maximizes the plasma rotation. NSTX.

A similar study was executed looking for n=2 error fields. The EFC coils were configured to yield an n=2 spectrum, and current levels of 250, 500, and 1000 A were applied. It was found that no EFC current level or phase of the applied n=2 field resulted in improved performance. As illustrated in Fig. 5.7, the rotation was reduced across the entire profile for all cases with 500 & 1000A applied n=2 field. Additionally the discharge duration was shortened by all phases of the applied n=2 field, usually due to the development of an RWM at reduced plasma rotation. These results indicate that n=2 error fields, if present, are sufficiently small that there is no benefit from correcting them.

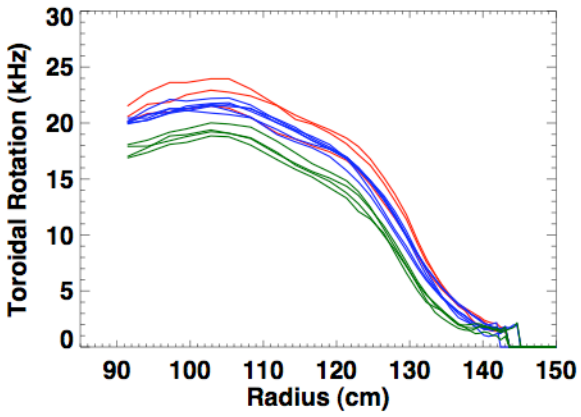

Fig 5.7 Rotation profiles with 0A (red), 500A (blue), and 1000A (green) of current in the n=2 configuration of the RWM coils. Different blue and green curves correspond to different phases of the applied n=2 field. NSTX.

5.5. RESONANT BRAKING IN DIII-D (N=1)

5.5.1. Introduction

Resonant magnetic field perturbations are to be avoided in a burning plasma because of the strong braking effect upon toroidal rotation, obviating the beneficial effects of plasma rotation and potentially locking the plasma to the perturbation, leading to a disruption. Experiments in 2008 in DIII-D have further clarified the role of plasma rotation itself, and the plasma stored energy upon this potential locking phenomenon.

Additional details will appear in the publication cited in Appendix B.10.

5.5.2. Experimental Results

The application of external n=1 magnetic fields leads to a decrease of the plasma rotation. If the magnetic perturbation is sufficiently large, the resulting braking causes a bifurcation in the torque balance. Once the torque balance is lost, the rotation collapses and the externally applied field penetrates and drives a magnetic island, which is consistent with a loss of shielding currents at low plasma rotation. The characteristics of resonant braking and the resulting n=1 error field threshold in Ohmically heated, low β plasmas [30] and NBI heated, high β plasmas [31] are similar. The observed decrease of the tolerance to externally applied n=1 fields with increasing β is explained by the dominant role of the plasma response in the magnetic braking. Fig. 5.8 compares two H-mode discharges with the same NBI torque but different values of β_N. While the tolerance to externally applied fields $\left(\propto I_{I-coil}\right)$ of the discharge with the higher value of β_N is smaller, the rotation collapse occurs at the same plasma response B_p^{plas}. The plasma response is caused by a resonant interaction of the externally applied n=1 field with a stable n=1 kink mode [32] and increases with β with the increase accelerating above the no wall ideal MHD stability limit, where the ideal MHD stable kink mode

converts to a kinetically stabilized resistive wall mode. Accounting for the plasma response actually leads to an error field threshold in H-mode plasmas (with low NBI torque) that is consistent with the linear density scaling of the locked mode threshold found in Ohmically heated, low-density, low β plasmas.

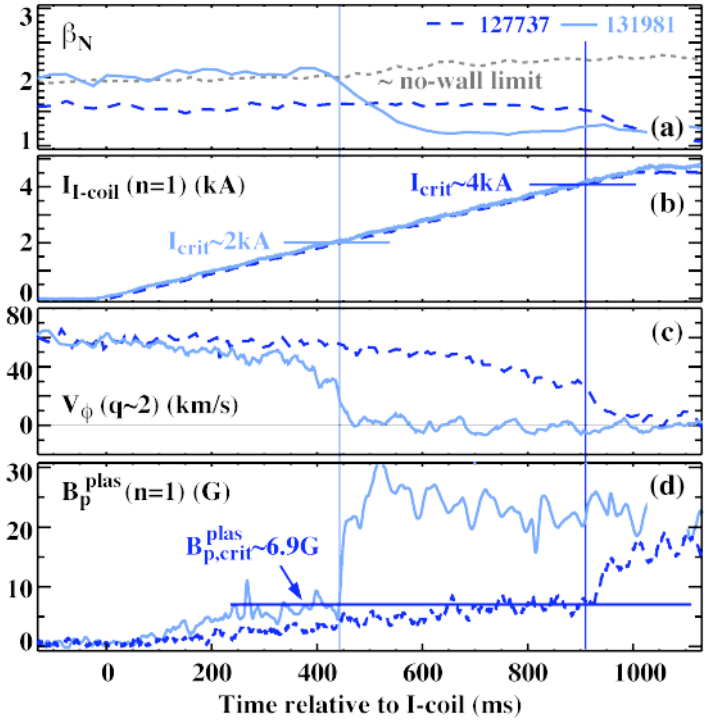

Fig. 5.8. At constant T_{NBI}≈ 1.8 Nm (solid blue) the discharge (131981) with the higher β_N (a) displays a lower tolerance against n = 1 field asymmetries applied with the I-coil (b) than the discharge with a moderate β_N (dashed blue 127737). The collapse of the toroidal rotation V_ϕ (c) occurs at approximately the same amplitude of the n=1 plasma response B_p^{plas} (d). DIII-D.

The braking torque from externally applied n=1 fields and the resulting plasma response is calculated from the global torque balance in quasi-static n=1 braking experiments. At the lower values of the plasma rotation (<30krad/s when evaluated at the q=2 surface), the magnetic braking torque is found to increase with decreasing rotation, which is consistent with a resonant magnetic braking torque [33] and thought to be the cause for the bifurcation in the torque balance. However, at higher rotation values the magnetic braking torque is found to increase with increasing rotation, which is characteristic for a non-resonant braking torque. The importance of both, resonant and non-resonant components of the perturbed magnetic field in braking the plasma rotation leads to a decrease of the tolerance to resonant fields and a diminished benefit of increasing the NBI torque in order to increase the error field tolerance.

Since the n=1 braking largely determines the error field tolerance, its β dependence, which is not included in empirical scaling laws [34], has to be taken into account in order

to obtain realistic error field tolerances for high β scenarios in ITER. However, the measurable increase of the plasma response with β and the rigid response to externally applied fields can be exploited for "dynamic" correction (i.e. with slow magnetic feedback) of the amplified component of the error field using correction coils with a simple geometry.

6. BOUNDARY CONDITION

6.1. INTRODUCTION

One model for intrinsic rotation is that there is some mechanism that provides a torque to the boundary surface of the plasma, which then propagates inward under the transport processes of diffusion, and the momentum pinch velocity (See Section 4.1). There is presently no model for the boundary condition for intrinsic rotation. No theory will be able to predict an absolute rotation profile without knowing the boundary condition.

In H-mode plasmas a transport barrier is formed near the plasma boundary that produces a sharp density gradient, relative to the drift orbit width of the ions, called the density pedestal. Such a regime falls outside the assumptions of the standard neoclassical theory. It is possible that orbit width effects in this region establish the boundary condition for intrinsic rotation. As such, it is very important to measure the detailed properties of this pedestal region, and especially the velocity profiles.

6.2. E_R WELL STRUCTURE AND SCALING IN C-MOD

6.2.1. Overview

For the first time detailed measurements of the electric field well [35] in the pedestal region of H-mode discharges have been made in C-Mod. The values obtained are very large as compared with other tokamaks and hopefully will provide new insight into the scaling of the H-mode pedestal parameters with the addition of these data from the high magnetic field, high density and smaller machine size regime. Since other C-Mod experiments indicate that the source of intrinsic rotation originates at the edge, these measurements will also help identify such a source.

6.2.2. Experimental Results

A new high-resolution charge-exchange recombination spectroscopy diagnostic utilizing intrinsic B^{+5} ions has enabled the first measurements of the radial electric field in the C-Mod edge plasma. These observations, made in torque-free pedestals, provide for important comparisons with other devices and offer new challenges for theory and simulation. Qualitatively, the field structure observed on C-Mod is very similar to that observed on other devices [35]. Quantitatively, the small C-Mod E_r well widths ($\sim$ 5 mm) suggest a scaling with machine size, while the observed E_r well depths (up to 300kV/m) are unprecedented – over twice as deep as on other devices. E_r is computed from the radial force balance equation for the B^{+5} ions, with the poloidal velocity of B^{+5}

found to be the dominant term, contributing 200kV/m transiently after L-H transitions and up to 80 kV/m during steady state H-modes. This differs from measurements made on other machines, in which the diamagnetic term is dominant. The radial electric field during EDA H-modes is steady in time, as shown in Fig. 6.1, while a clear evolution of the E_r well depth is observed in ELM-free H-modes, with the depth of the well decaying, as the H-mode pedestal degrades due to increases in radiated power. Surprisingly, it is the boron VxB term in the force-balance equation, not the diamagnetic term, which decays during ELM-free H-modes. In fact, the diamagnetic term is observed to make a fixed contribution to the E_r well depth in all types of H-modes. The diamagnetic term for the main ions can be estimated from Thomson scattering profiles and is found to equal E_r computed from B^{+5} radial force balance. This assumes that $T_i = T_B$, which is justified on the basis that T_B is measured to be equal to T_e throughout the pedestal. An important implication, and support for neo-classical theory, is that the main ion VxB contribution to E_r is negligible. The depth of the H-mode edge E_r well is found to be strongly correlated with overall energy confinement properties of the plasma. Shown in Fig. 6.2 is the radial electric field well depth as a function of H-factor, for EDA and ELM-free H-mode plasmas.

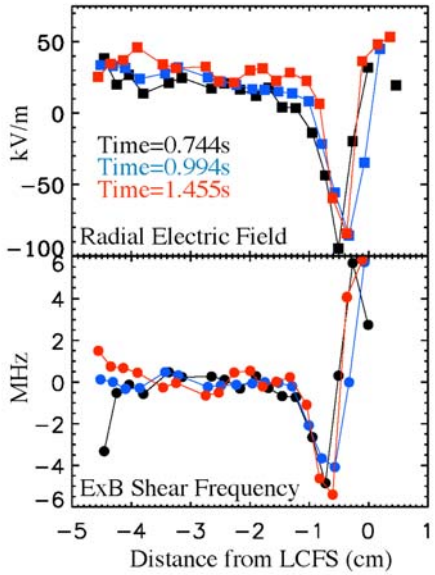

Fig. 6.1. Edge Er and shearing rate profiles for EDA. C-Mod.

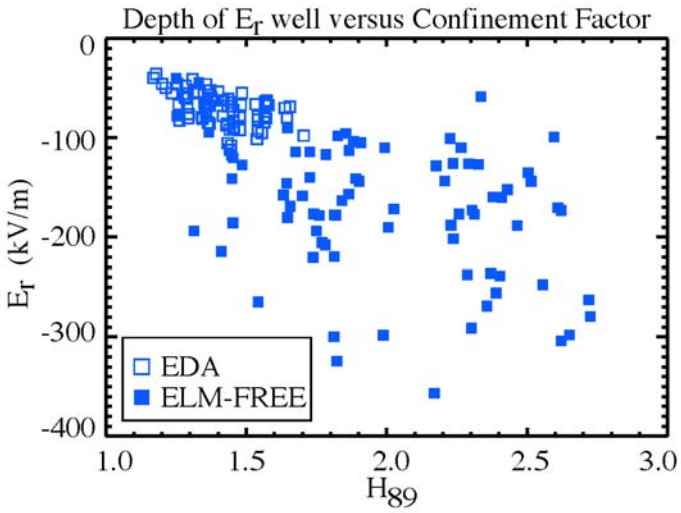

Fig. 6.2. The Er well depth as a function of H-factor. C-Mod.

6.3. INTRINSIC BOUNDARY CONDITION IN DIII-D

6.3.1. Overview

A number of theories exist that offer at least a qualitative explanation of intrinsic rotation. An unknown in these theories is invariably the boundary condition that should be placed upon the intrinsic velocity at the last closed flux surface (LCFS). Without the boundary condition the theory cannot make a prediction of the absolute intrinsic velocity, or rotation profile.

In DIII-D we have experimentally measured the intrinsic velocity in the pedestal region of ECH and Ohmic H-mode discharges, those without perturbative NBI momentum drive. We find that the velocity, V_ϕ, is in the direction of the plasma current, co-Ip, and is roughly proportional to the local ion temperature, T_i. A simple model of edge orbit loss of thermal ions reproduces this scaling. This is a model without collisions. However, a recent particle simulation of a DIII-D NBI-driven discharge, with collisions included, also invokes thermal ion orbit loss to explain a co-Ip velocity in the pedestal region [36]. So we believe that collisions will not wash out the effect. The ions are lost from a small region of phase space, through the X-point of a poloidally diverted discharge. The resultant scaling for this intrinsic velocity boundary condition model is

$$V_\phi^{edge} = T_i / LB_\theta \qquad (1)$$

which is of so-called diamagnetic form [37]. Here, B_θ is the poloidal magnetic field strength and L has the units of length.

The proportionality $V_\phi \sim T_i$ is found experimentally to extend inward, beyond the range that ion thermal orbit loss is effective. We postulate that a momentum pinch velocity, V_{pinch}, proportional to the ion temperature gradient could result in this temperature scaling inside the pedestal.

Additional details will appear in the publication cited in Appendix B.11.

6.3.2. V_ϕ Scaling and Orbit Loss

In Figure 6.3 we show measurements of V_ϕ in the pedestal region vs T_i at the same location for the intrinsic rotation database in DIII-D. Data from five spatial locations are shown. All locations span a width of only 5 cm, with the full width of the pedestal ~ 1.5 cm. The open and closed circular symbols are inside the top of the pedestal, while the others span the pedestal. The approximate linear proportionality to T_i is apparent.

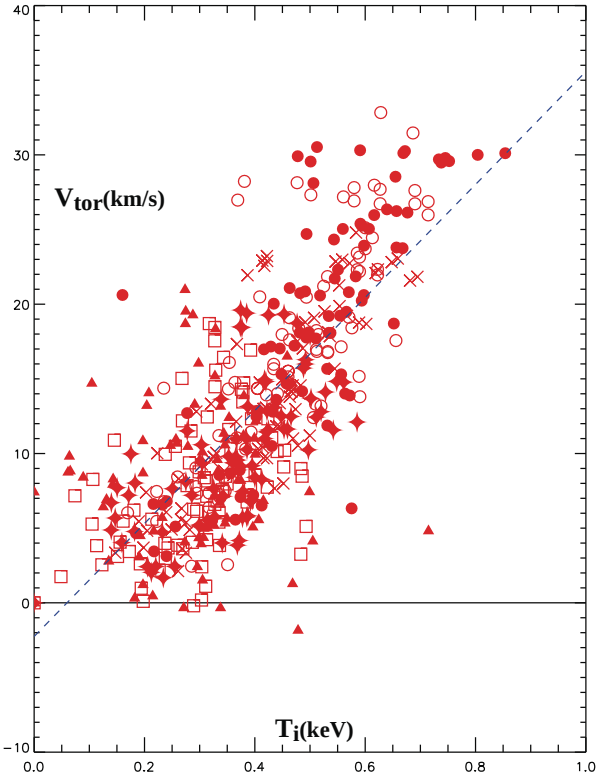

Fig. 6.3. V_ϕ vs T_i for intrinsic rotation conditions in DIII-D, for $\rho > 0.8$. The line is a least squares fit. DIII-D.

In Fig. 6.4 we show the results of the thermal ion orbit loss model for the conditions of one particular discharge point at the location of the inner half-width of the pedestal there. First, note the approximate linearity of the computed V_ϕ with T_i. The horizontal and vertical lines show the actual measurement of V_ϕ and T_i for this data point.

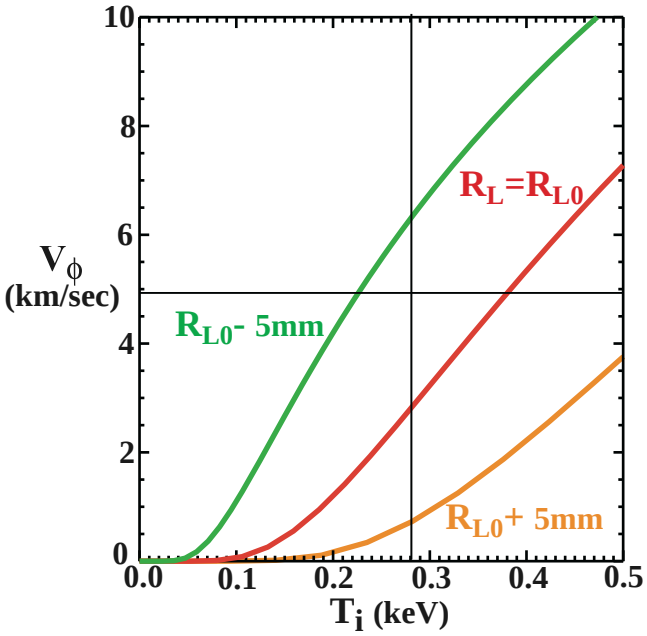

Fig. 6.4. The middle line uses the result from the thermal ion loss calculation and computes an absolute value for V_ϕ near the top of the H-mode pedestal. The two other lines compute an absolute value using a different location of the LCFS, 5 mm closer to the measurement channel (green online), and 5 mm further away (orange online). The horizontal and vertical lines indicate the actual measurement values for this condition. DIII-D.

A critical parameter in the ion orbit loss model is the distance between the orbit starting point, taken to be the measurement location, and the LCFS. In DIII-D, studies have shown the typical error in location of the LCFS with the equilibrium-fitting code is +/- 5 mm [38,39]. This error is large enough to introduce a significant uncertainty in the loss-model determination of an absolute velocity value. The middle line in Fig. 2 uses the LCFS determination from the fitted equilibrium. The two other lines use a value + and – 5mm different, respectively. Within this range of uncertainty the value of V_ϕ is well approximated.

It is our hope that rigorous theoretical work, and particle simulations will be brought to bear on this issue of thermal ion orbit loss establishing the intrinsic velocity boundary condition. Additionally, in spite of the quantitative difficulty of predicting an absolute velocity due to the LCFS measurement, it is hypothesized that the scaling of such a boundary condition will be experimentally verifiable.

6.3.3. A Momentum Pinch Model

The $V_\phi \sim T_i$ proportionality seen in Fig. 6.3 goes in beyond the point where thermal ion orbit loss is effective. We postulate that a momentum pinch velocity, $V^P \equiv V_{pinch}$, proportional to the ion temperature gradient is responsible for carrying this scaling inward spatially.

It can be shown in this spatial region that the flux of toroidal momentum, Γ_ϕ, is proportional to $\Gamma_\phi \sim -\chi_\phi \partial V_\phi / \partial r + V^P V_\phi$, where χ_ϕ is the momentum diffusivity, and r is the minor radius coordinate. A state of local intrinsic velocity inside the plasma means that there is no interior momentum generation, or flux. So, $\Gamma_\phi = 0$ there. If $V^P / \chi_\phi = k(\partial T_i / \partial r)/T_i$, and there are theories of a turbulence-driven pinch that give this result [40,41] in the limits that apply to these experimental conditions, then the velocity solution is $V_\phi = V_\phi(a)\left[T_\mathrm{i}/T_\mathrm{i}(a)\right]^\mathrm{k}$, where k is a constant, and $V_\phi(a)$ is the boundary value. To match our experimental measurements, k must be reasonably close to unity.

If this model of the turbulent pinch has some validity, then understanding the turbulence drive must give a picture that fits with the Rice scaling, in that the increase in V_ϕ moving in from the pedestal ultimately results in a peak that fits the Rice scaling in DIII-D.

7. EFFECTS OF ROTATION - STABILITY

7.1. SUMMARY

A wide variety of MHD instabilities has been shown to be modified strongly by rotation and/or rotation shear. Studies have been carried out in controlled fashions, utilizing co + counter injection and magnitude of error fields in DIII-D and n=3 magnetic braking in NSTX. Using both techniques, it was found that both 2/1 and 3/2 Neoclassical Tearing Modes have increased stability at larger rotation and rotation shear. The experiments in NSTX point to rotation shear as having the more dominant effect. These rotation and rotation shear effects, however, are only part of the story, as magnetic shear can also modify the tearing mode stability and structure.

High performance plasmas, with $\beta > \beta_{\text{no-wall}}$, have been produced at low rotation in both DIII-D and NSTX. In DIII-D, these plasmas were limited by NTMs rather than by RWMs. RWMs in DIII-D, however, can be triggered by perturbations such as Error Fields and ELMs. The growth of the RWMs at low rotation has been effectively mitigated through magnetic feedback stabilization techniques. Dedicated experiments in NSTX showed the importance of kinetic effects in stabilizing the RWM at low rotation, and also pointing out the effect of the complicated interplay between rotation and kinetic effects on RWM marginal stability. Simple viscous models of energy dissipation that produce scalar values of a critical plasma rotation frequency, Ω_{crit}, do not match observations, as marginal RWM stability in NSTX is at least related to the plasma rotation profile, and the RWM can be unstable at both high and low plasma rotation.

These results have important implications for ITER. The DIII-D results suggest that wall-stabilized scenarios in ITER could possibly tolerate low rotation as long as external and internal perturbations are avoided (e.g. low intrinsic error field, ELM mitigation) or corrected sufficiently well and sufficiently fast (e.g. with an active non-axisymmetric magnetic feedback system). Further, the kinetic effects that can dramatically modify the RWM stability are expected to be large at the low collisionalities of ITER. For the ITER steady state scenarios, the self-consistent kinetic model predicts a full stabilization of the RWM at very slow plasma rotation (less than 0.2% of the Alfvén speed at the plasma center) and moderately high plasma pressures $\left(C_\beta \le 0.4\right)$, which is only slightly less optimistic than the predictions by a perturbative approach.

Additional details will appear in the publication cited in Appendix B.12,13.

7.2. NTM THRESHOLD WITH ROTATION IN NSTX (2/1) AND DIII-D

Experiments on DIII-D have utilized its balanced neutral beam injection capability to explore the change in the main pressure limit for the ITER baseline scenario with injected torque. This limit arises from a flux tearing instability termed the 2/1 Neoclassical Tearing Mode (NTM). The DIII-D data shows a pronounced effect with the limit in normalized pressure, β_N, falling from the high values attained with strong co-injection (as most present tokamaks usually operate) to much lower values at more ITER-relevant torques, where the pressure limit found to be just greater than the ITER operating point of $\beta_N = 1.86$. To understand the physics, scalability and potential for control of this mode, experiments were extended in 2008 to strong 'counter injection' (where beams inject in the opposite direction to the plasma current). The results show that torque (or plasma rotation) is not simply stabilizing to tearing modes – with increasing counter torque, the limit first falls further before recovering somewhat (Fig. 7.1). The behavior favors a model in which sheared rotation modifies the tearing mode structure and stability, adding to, or cancelling, a similar effect arising from the magnetic shear. This suggests that increases in the pressure limit might be achievable by further manipulation of the current profile.

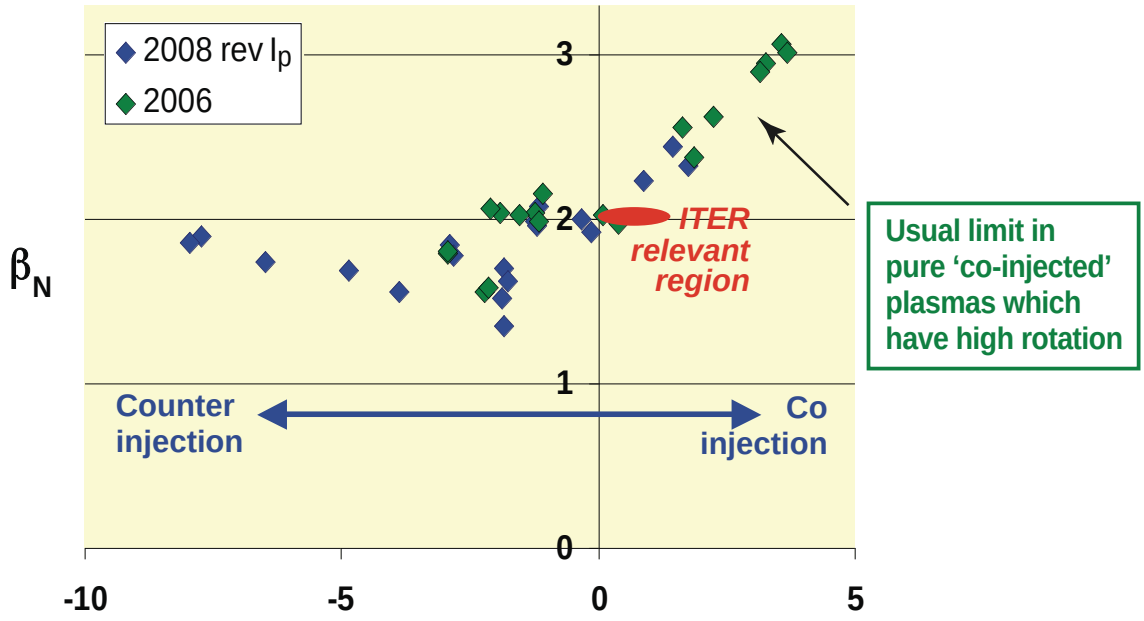

Figure 7.1 Preliminary results showing the trend in the 2/1 NTM pressure limit as torque injection to the plasma is varied for an ITER baseline-like plasma in DIII-D

Further experiments (not shown), using these plasmas, have also explored their error field sensitivity in order to provide a basis for revised error field correction requirements at low torque and intermediate β_N, relevant to the ITER baseline. These show an

increased sensitivity to error field as the threshold for the 2/1 NTM is approached by either torque or β_N variation. Thus error field correction requirements appear to be increased at low torque or high β_N.

Plasma rotation and/or rotation shear has also been considered to play an important role in determining the stability of Neoclassical Tearing Modes (NTMs). Results from DIII-D using mixed co/counter balance show that for the 3/2 mode, the saturated m/n=3/2 neoclassical islands are larger when the rotation shear is reduced. Furthermore, the onset β_N for the 2/1 mode is lower at reduced rotation and rotation shear.

Experiments in NSTX have studied the onset conditions for the 2/1 mode, as a function of rotation and rotation shear, where applied n=3 magnetic fields leading to rotation braking have been utilized to slow rotation. By studying many discharges with a range of braking levels and injection torques, a wide variety of points in rotation/rotation shear space have been achieved. Additionally, all NTM relevant quantities, such as the rotation shear and bootstrap drive for the mode, have been calculated using correct low-aspect ratio formulations.

The results of this exercise are shown in the Fig. 7.2, where the bootstrap drive at NTM onset is plotted against a) plasma rotation frequency at q=2, and b) local rotation shear at q=2; larger values of drive at mode onset imply increased stability. The color scheme is related to the triggering mechanism: the modes are observed to be triggered by energetic particle modes (EPMs, orange points) or Edge Localized Modes (ELMs, blue points), or in some cases grow without a trigger (purple points). Considering frame a), it is difficult to see any meaningful trend in the onset threshold with rotation, either within each trigger type or considering all of the points as a group. This is in contrast to the data in b), where the onset NTM drive is plotted against the rotation shear at q=2. The entire set of points shows increasing drive required at larger local flow shear. Furthermore, the colored lines show that within each trigger type, the onset threshold depends on the local rotation shear, with EPMs triggering the modes at the lowest drive, ELMS at intermediate levels, and the triggerless NTM occurring at the largest bootstrap drive. These and other NSTX results, coupled to DIII-D measurements, imply that sheared rotation, and its synergistic coupling to magnetic shear, can strongly affect tearing mode stability.

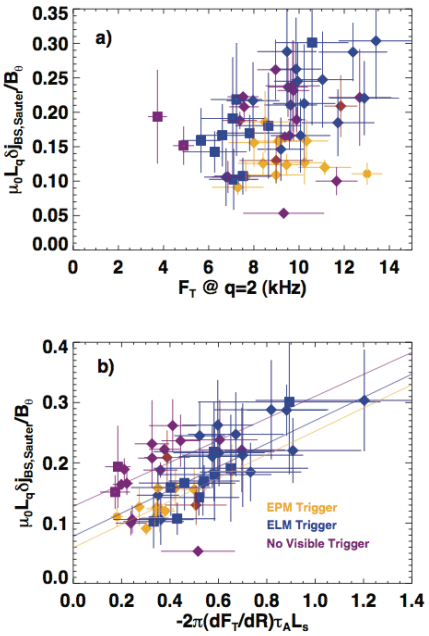

Fig. 7.2. Bootstrap drive plotted as a function of rotation (a) and rotation shear (b). NSTX.

7.3. SIMULTANEOUS RWM AND NTM STABILIZATION PHYSICS AT LOW ROTATION IN DIII-D

Recent DIII-D experiments have demonstrated wall-stabilization with values of the toroidal plasma rotation (measured from CVI emission) at the q=2 surface of only 0.1% of the Alfvén velocity, which is well below the rotation thresholds previously reported for similar low NBI torque plasmas [42], Fig. 7.3. In these discharges approximately 2 MW of ECCD at the q=2 surface suppresses the onset of a non-rotating n=1 mode, which indicates that the operation at high β and low rotation is usually limited by a (locked growing) m/n=2/1 neoclassical tearing mode (NTM) rather than an RWM [see Sec. 7.2 "NTM threshold with rotation in NSTX and DIII-D"]. This conclusion is also supported by the ineffectiveness of magnetic feedback to modify the growth rate of the mode let alone stabilize it. The observed stability of the RWM at low plasma rotation in DIII-D is consistent with the modeling of kinetic effects using a perturbative approach [43].

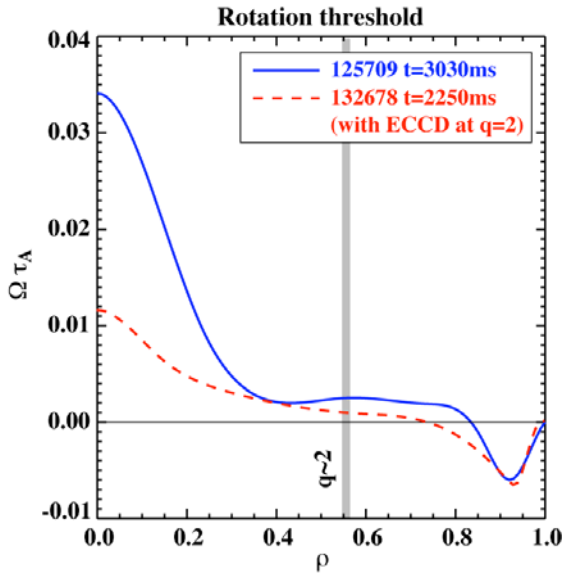

Fig. 7.3 Rotation thresholds in discharges, where β exceeds the no-wall limit, with (132678) and without localized ECCD at the q=2 surface (125709). DIII-D.

While a low rotation, wall-stabilized plasma state has been demonstrated, steady-state operation in such a regime is not unconditionally guaranteed as other modes such as ELMs and q=2 fishbones can couple to the RWM. It is thought that similar to resonant field amplification of externally applied non-axisymmetric "error" fields [44], these localized modes can be amplified by the marginally stable RWM leading to large non-axisymmetric perturbations of the plasma. However, ELMs are also seen to lead to growing perturbations that are consistent with an unstable RWM indicating the possibility of a non-linear coupling between ELM and RWM. Magnetic feedback has been effective in mitigating the non-axisymmetric perturbations and improve discharge performance.

7.4. PARAMETRIC DEPENDENCE OF RWM STABILITY ON PLASMA ROTATION AND COLLISIONALITY

RWM passive stabilization has been investigated on NSTX, with results summarized by Sontag et al. [45]. While simple RWM models [46] can qualitatively describe RWM dynamics, dispersion relations of these models do not fully describe RWM marginal stability in NSTX. The dependence of marginal stability on ω_ϕ is especially profound. Simple viscous models of energy dissipation that produce scalar values of a critical plasma rotation frequency, Ω_{crit}, do not match observations, as marginal RWM stability in NSTX is at least related to the plasma rotation profile, and the RWM can be unstable at both high and low plasma rotation.

Kinetic modifications to ideal stability are examined including the effect of trapped and circulating ions, trapped electrons, and Alfven damping [47] in an attempt to

reproduce NSTX observations. Variation of the plasma rotation from the experimental marginally stable equilibrium reconstruction shows reduced stability at intermediate and low plasma rotation, rather than a simple critical rotation threshold. This is shown by varying the experimental rotation profile $\omega_\phi{}^{\exp}$ and computing $\gamma\tau_w$ for the variations. A stability diagram is produced in which contours of constant $\gamma\tau_w$ are plotted on a plot of $Im(\delta W_K)$ vs. $Re(\delta W_K)$ in Fig. 7.4. The region of $\gamma\tau_w > 0$, which is theoretically unstable to the RWM, is highlighted. The rotation profile is varied self-similarly from 0 to 2 times the experimental profile. As the rotation is theoretically varied, the stability is altered. Starting from twice the rotation found experimentally, the plasma stability decreases as plasma rotation decreases toward the point "1.0", which represents the measured experimental profile. This point, which is experimentally observed to be on the verge of instability, is predicted to be close to marginal $(\gamma\tau_w < -0.1)$. As ω_ϕ is reduced further, the plasma becomes more stable at $0.8\omega_\phi{}^{\exp}$ with $\gamma\tau_w > -0.2$ and then stays approximately constant down to $0.6\omega_\phi{}^{\exp}$. For low rotation $\left(< 0.4\omega_\phi{}^{\exp}\right)$, the plasma is predicted to be unstable. This is consistent with the general NSTX experimental observation that very low global rotation at $\beta_N > \beta_N{}^{no-wall}$ is typically unattainable without active n = 1 RWM feedback control.

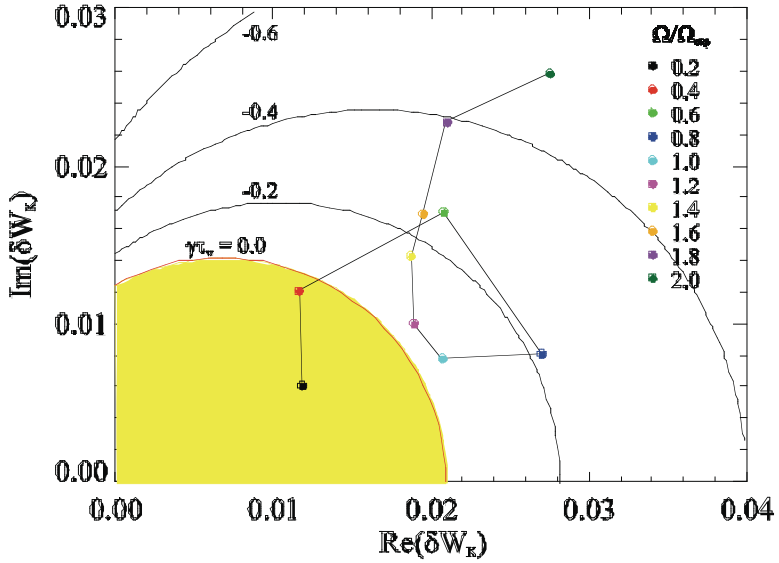

Fig. 7.4. Effect of plasma rotation on n = 1 RWM stability for plasma 121083 at 0.475s. The markers are $\mathrm{Im}(\delta W_K)$ plotted vs. $\mathrm{Re}(\delta W_K)$ for various rotation profiles, self-similarly scaled from the experimental profile. NSTX.

Variation of plasma collisionality, ν, from the experimental equilibrium alters the dependence of stability on rotation. Figure 7.5 shows analogous trajectories to Fig. 7.4, but with electron and ion temperatures halved/doubled, producing increased/decreased collisionalities by a factor of 5.7 while maintaining constant plasma pressure. Increased collisionality simplifies the dependence of stability on ω_ϕ, making the trajectory appear more like it has a single critical rotation profile for stability. This might be expected, as

higher ν decreases the relative importance of the kinetic resonances. Decreasing collisionality produces an opposite effect. As ω_ϕ is decreased, there is a broader reversal of $\gamma\tau_w$ from decreasing to increasing stability, marginal stability occurs at higher plasma rotation than in the actual experiment, and the trajectory shows stability at low plasma rotation.

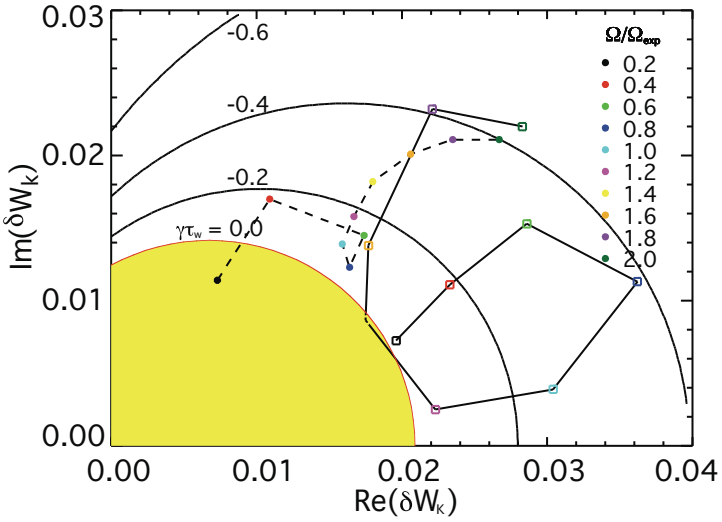

Fig. 7.5. Effect of plasma collisionality (through variation of temperature and density) on n=1 RWM stability for plasma 121083 at 0.475 s. Solid circles/dashed line indicates ω_ϕ variation at increased ν, while open squares/solid line show the ω_ϕ variation at decreased ν. NSTX.

8. EFFECTS OF ROTATION - CONFINEMENT

8.1. SUMMARY

Various means have been employed on both NSTX and DIII-D to vary the $E \times B$ shear, as well as magnetic shear, and relate these to variations in transport and turbulence. n=3 magnetic braking was used on NSTX to create a series of H-mode discharges with a factor of three range in rotation and rotation shear in the outer regions of the plasma. While the total confinement did not change over this range, local transport, especially χ_i, increased with decreasing rotation shear, going from near neoclassical to strongly anomalous $\left(\sim 4\chi_{i,neo}\right)$. This result is consistent with $E \times B$ shearing suppression of low-k turbulence, as determined from linear gyrokinetic calculations. Also, the location of maximum $E \times B$ shearing rate was found to coincide with the location of the ion internal transport barrier in L-mode discharges. The $E \times B$ shearing rate was modified in DIII-D using different combinations of co and counter-NBI sources, and this was coupled to variations in magnetic shear produced through different current ramp rates and timing of auxiliary heating. While the large $E \times B$ shear cases led to a sustained improvement in confinement, similar discharges with low $E \times B$ shear did not exhibit sustained improvement, although transient improvements, associated with integer $q_{\min}$, were observed.

The results indicate that both $E \times B$ and magnetic shear are important for optimizing confinement in fusion devices, including ITER. What is critical is to extend the high $E \times B$ shear over a region as large as possible, while at the same time tailoring the current profile to achieve $q_{\min}$ at or near an integer value, to realize the maximum confinement improvement.

8.2. MAGNETIC BRAKING IN NSTX

NSTX is equipped with the means of applying low-n (n=1 to 3) magnetic fields to the plasma edge using a set of six coils situated on the midplane outside the vacuum vessel. This set of coils has been used in an n=3 configuration to apply non-resonant magnetic perturbations to modify the plasma rotation. The maximal torque from these fields, as inferred by local changes in plasma rotation, is observed to be near R=1.3 m, which is in agreement with calculations of the torque due to neoclassical toroidal velocity in the presence of these applied perturbed fields. By changing the rotation and rotation profile (gradient) locally, it is possible to study their effect and relation to both the global energy confinement and local heat transport properties of the plasma.

A series of H-mode discharges in which the magnitude of the applied n=3 field was varied is shown in Fig. 8.1. The top panel shows the current through one of the midplane coils. The rotation at R=1.35 m is seen to change with the application of the n=3 fields (second panel from top), with each discharge reaching a new rotational equilibrium in this MHD- and ELM-free period (bottom two panels). The rotation ranges from 25 km/s to close to 80 km/s over the range of applied n=3 fields. The plasma stored energy (middle panel, note the suppressed zero in the ordinate) shows little variation with the different levels of plasma rotation.

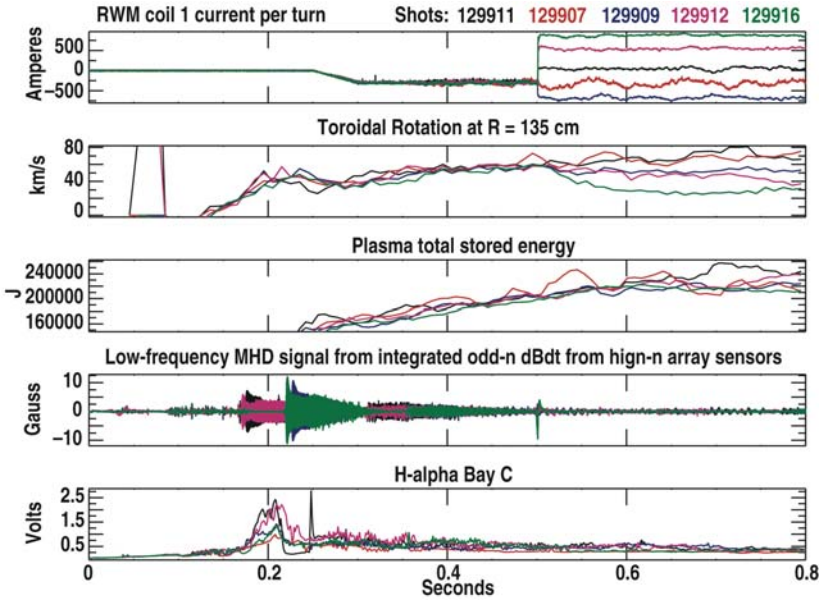

Fig. 8.1. Time traces for 5 H-mode discharges with application of different levels of n=3 braking fields. Shown from the top is the n=3 coil current, toroidal rotation at R=1.35 m, plasma stored energy calculated by EFIT, low-frequency MHD activity, and the D_α traces. NSTX.

The change in rotation and rotation shear is maximum, however, in just a limited spatial range of the plasma, in these cases in the region of $r/a \sim 0.6$ to 0.9. Consequently, it is not readily apparent that a change in these parameters would affect the plasma on a global scale. Fig. 8.2 shows the ion (left panel) and electron (right panel) thermal diffusivities for three representative discharges that span the range from minimum (green) to maximum (red) rotation (2 to 6×10^5 rad/s) and rotation shear (0.2 to 2.4×10^3 rad/s/cm) in the region near $r/a = 0.75$, obtained by maximum and no braking respectively. The thermal diffusivity values in the region near r/a=0.75 to 0.85 show a clear reduction with increasing Ω and $\nabla\Omega$. This is particularly true in the ion channel, where there is a factor of almost three difference between the maximum and minimum Ω and $\nabla\Omega$ cases. For the ions, the ratio of $\chi_i/\chi_{i,neo}$ increases from 1.2 to 3.9 with decreasing Ω and $\nabla\Omega$.

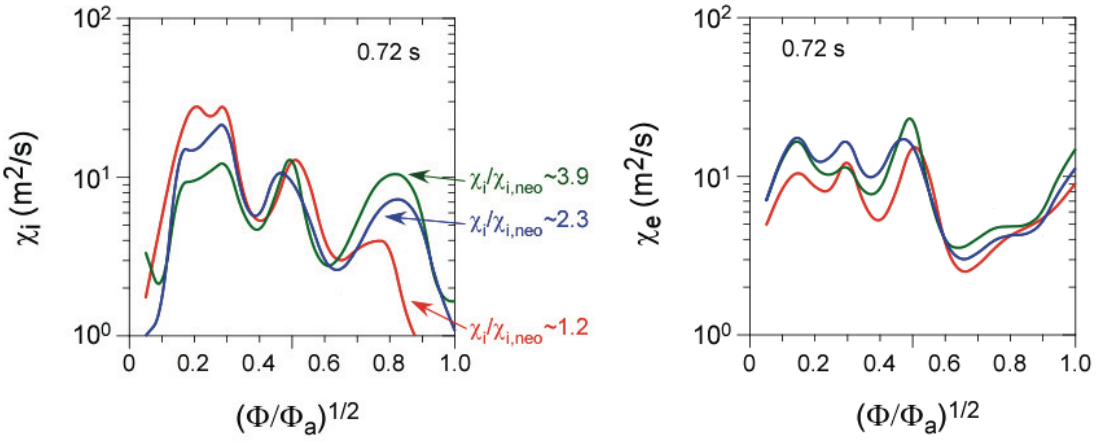

Fig. 8.2. Ion (left) and electron (right) thermal diffusivities over a range of Ω and $\nabla\Omega$. The green and red curves are from the discharges with minimum and maximum Ω and $\nabla\Omega$. NSTX.

This dependence can be understood in terms of the degree of suppression of low-k turbulence by rotation $(E \times B)$ shear. Linear GS2 gyrokinetic calculations of the growth rates of low-k turbulence were carried out in the extreme cases, those with minimum and maximum Ω and $\nabla\Omega$. While the linear growth rates for the two cases are similar the $E \times B$ shearing rates are not, with the maximum Ω and $\nabla\Omega$ case having $\omega_{E\times B}$ a factor of five higher than the linear growth rate, and the minimum case having the two rates comparable. This result suggests more of a reduction in the low-k (ITG/TEM) turbulence in one case than the other, and it is consistent with the increase $\chi_i/\chi_{i,neo}$ from ~ 1 to ~ 4 going from the case with $\omega_{E\times B} >> \gamma_{lin}$ to the one with $\omega_{E\times B} \sim \gamma_{lin}$.

8.3. DIII-D EXPERIMENT COMPARING $E \times B$ WITH MAGNETIC SHEAR

The theory of turbulent plasma transport indicates that shear in the $E \times B$ flow and shear in the magnetic field can both affect the level of turbulence and turbulence-driven transport. On DIII-D, an experiment was done to try to separate the effects of equilibrium $E \times B$ shear and magnetic shear on turbulence and turbulent transport. Co- plus counter-neutral beam injection were used to alter the toroidal rotation, thus changing the radial electric field and the $E \times B$ shear. In addition, current ramping was used to modify the magnetic shear. The long term goal is to obtain data on six different conditions: low magnetic shear, strong negative magnetic shear and strong positive magnetic shear each with two different levels of $E \times B$ shear. In this experiment, the low shear and positive magnetic shear cases were obtained with two different levels of $E \times B$ shear. Low shear was created by rapid current ramp up in a plasma with early heating with electron cyclotron waves (ECH) and neutral beam injection (NBI). This is an extension of the technique utilized by Austin et al [48]. The addition of ECH produced a larger radius for the minimum q location, which facilitates the measurement using beam emission

spectroscopy (BES). By changing the neutral beam torque in these plasmas, we were able to create some shots with rapid toroidal rotation, which leads to significant equilibrium $E \times B$ shear, and other shots with little toroidal rotation, which leads to negligible $E \times B$ shear. Previous work with low magnetic shear, high rotation plasmas exhibited stepwise improvements in confinement when q passed through low order rational values [48]. The low shear, low rotation plasmas are particularly interesting, since transient confinement improvement when $q_{\min}$ reaches integer values are still seen; however, the sustained confinement improvement characteristic of large equilibrium $E \times B$ shear is not seen. The transient confinement improvement has been ascribed to the effects of turbulence driven zonal flows [49]. Changes in the level of microturbulence and in the poloidal propagation speed the turbulent eddies are associated with the transient decrease in confinement and that the location of these tracks the location of the $q_{\min} = 3$ surface in these shots. In addition, we see that the change in the turbulent eddy poloidal velocity can actually precede the change in turbulent intensity at some locations. Further analysis of these results and the high magnetic shear cases is in progress.

8.4. NSTX EXPERIMENT ASSESSING ROLE OF EXB AND MAGNETIC SHEAR ON FORMATION OF ION AND ELECTRON INTERNAL TRANSPORT BARRIERS

Studies of both electron and ion internal transport barriers have been carried out in NSTX in L-mode plasmas. The relation of the magnetic shear and the $E \times B$ shear to the ion and electron ITBs were studied in these L-mode plasmas by using different plasma current ramp rates and neutral beam injection timing in the early phases of the discharge to vary the magnetic shear, and by using different combinations of the neutral beam sources and their timing to vary the $E \times B$ shear. An example from one of these discharges is shown in Fig. 8.3, and typifies the robust relations observed. Very clearly, the location of the maximum of the $E \times B$ shearing rate profile (shown in the top panel) occurs at the same location as the minimum in the ion thermal diffusivity (bottom panel). The is also the location where $\chi_i / \chi_{i,neo}$ is closest to one. This location corresponds to the location of maximum ion temperature gradient, and thus gives the location of the internal ion transport barrier. The location of the electron internal transport barrier, as shown by the minimum in χ_e (the red curve in the bottom panel) always occurs inboard of the ion ITB, and corresponds directly to a minimum in the q-profile.

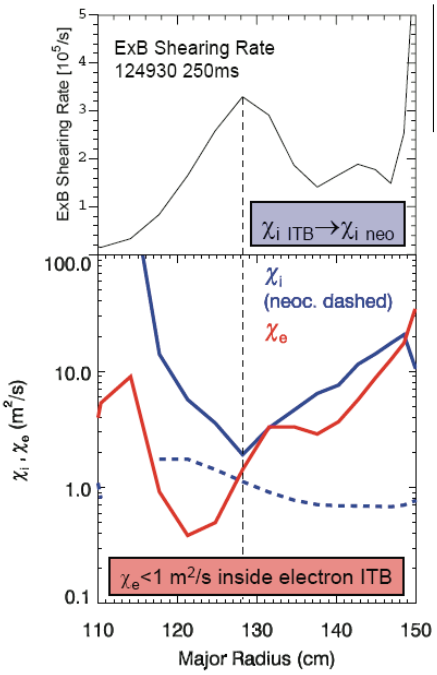

Fig. 8.3. $E \times B$ shearing rate (top panel) and thermal diffusivities (bottom panel) for an L-mode NSTX discharge, showing the correspondence between the locations of maximum shearing rate and ion Internal Transport Barrier.

9. OTHER EFFECTS OF ROTATION

9.1. EFFECTS OF ROTATION ON THE L->H POWER THRESHOLD IN DIII-D

9.1.1. Overview

In DIII-D the power threshold to obtain the transition to the high confinement H-mode has been determined to be a function of the toroidal rotation velocity, which is varied using the simultaneous co-Ip and counter-Ip directed neutral beam injection (NBI) capability. A positive result for ITER is that low toroidal rotation is found to have a lower power threshold than the high co-Ip toroidal rotation cases that dominate the past database for NBI-heated discharges. However, it is observed that the threshold power is greater for hydrogen, H+, discharges than for deuterium, D+. In ITER a H+ phase of operation will precede the D+ phase.

Additional details will appear in the publication cited in Appendix B.14.

These DIII-D variable velocity results will be carefully compared with the international database, and also H-mode power threshold experiments in C-Mod, in which the only heating method is rf, with relatively low toroidal velocity prior to the transition.

9.1.2. DIII-D Results

A set of experiments was performed to determine the H-mode power threshold as a function of the applied torque and for different heating methods (NBI and ECH). The H-mode power threshold was determined for many cases with increasing power steps at constant applied beam torque, but with different starting torques for the same set of plasma parameters and conditions. Only the plasma configuration was changed from upper single null (USN) to lower single null (LSN) plasmas, as shown in Fig. 9.1. The net threshold power is determined from the sum of the input power (NBI, ECH, and Ohmic) minus the core radiated power and the time derivative of the stored energy. The results of these scans are shown in Fig. 9.2. The H-mode power threshold exhibits a clear and significant increase with the applied beam torque of nearly a factor of 3 for the USN discharges at $\bar{n}_e = 2.4 - 2.7 \times 10^{19}$ m^{-3} (solid symbols) from about 2 MW with predominantly counter-injected beams (applied torque of –0.5 Nm) to about 5.5 MW with all co-injected beams (applied torque of about 4.1 Nm). An increase in threshold power with applied beam torque is also observed in LSN plasmas at the same target densities (open symbols), but is less pronounced, showing an increase of nearly a factor of 2 from about 1.7 MW (applied torque of –1.3 Nm) to about 3.1 MW (at applied torque of 2 Nm). The threshold power is lower for the LSN discharges with applied ECH when compared with only NBI heated discharges. For both LSN and USN discharges, the ECH plus NBI

heated discharges exhibit a slight increase in the threshold power with the input torque, but not as strong as the only NBI heated cases.

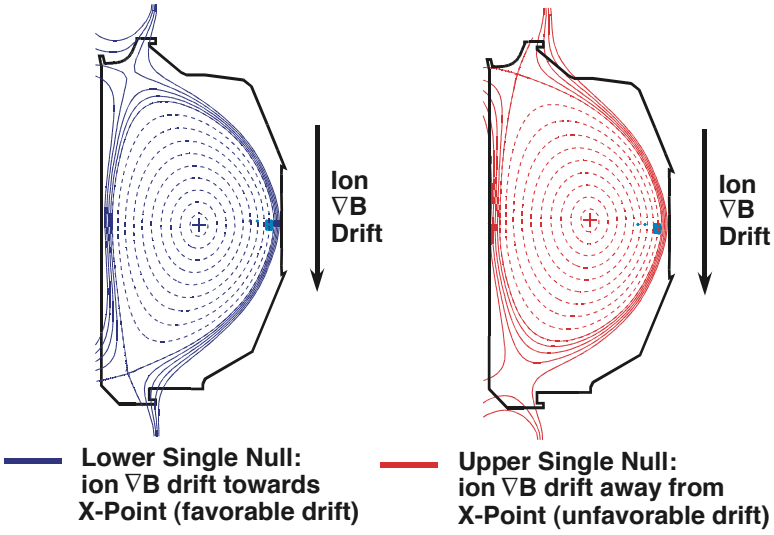

Fig. 9.1. Poloidal flux surface shapes for LSN and USN discharges used in DIII-D for this experiment.

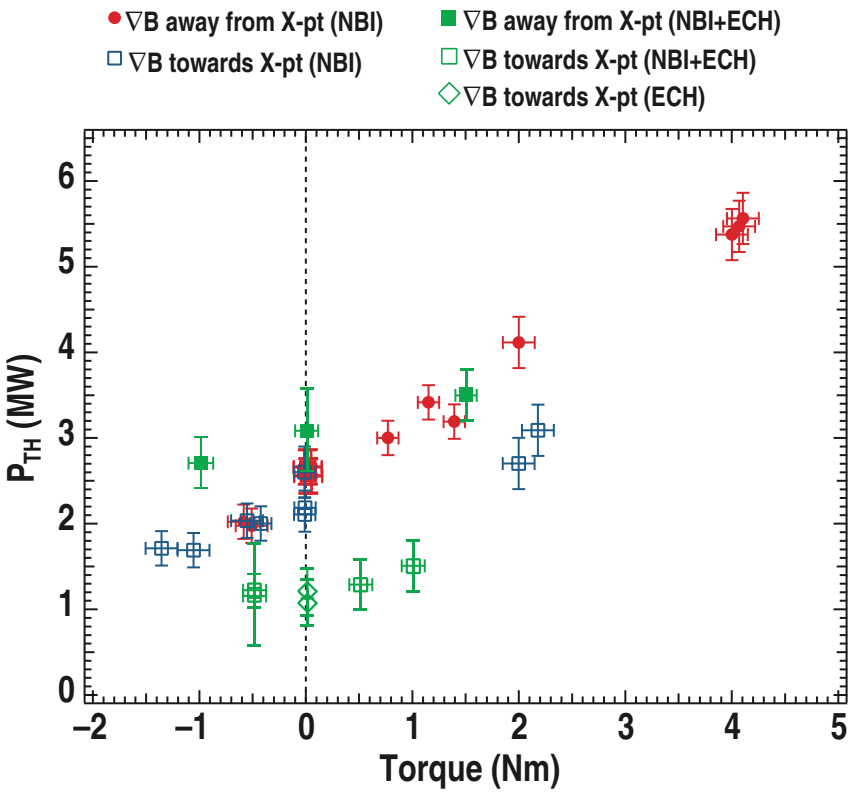

Fig. 9.2. The H-mode threshold power as a function of the input torque from neutral beams. The dependence is shown for plasma discharges biased in the upwards direction (USN) and for plasmas biased downwards (LSN). DIII-D.

The results shown in Fig. 9.2 clearly indicate a dependence of the H-mode power threshold on the applied beam torque. However, they do not, in themselves, reveal the important plasma quantity that may be influencing the threshold power behavior. In order to determine the role of any edge quantity, a detailed analysis of various quantities at the plasma edge was performed for many (a total of 9) scans shown in for Fig. 9.2. Such quantities included the evolution of the electron and ion temperatures and densities, the toroidal and poloidal rotation and the edge electron pressure in the L- mode prior to the H-mode transition. A key edge quantity that showed a clear correlation with the threshold power was the edge toroidal velocity. Figure 9.3 shows the dependence of the power threshold on this velocity measured 1 cm inside the location of the separatrix in the L-mode phase just before the H-mode transition. The toroidal velocity is not simply determined for one CER chord for all the cases, but is instead determined from the actual profile of the toroidal velocity at the plasma edge, from which the velocity value is taken at the location of 1 cm from the separatrix. The implications for ITER are favorable given the low rotation plasmas expected in ITER. However, the assumptions and extrapolations of the H-mode threshold power scaling laws to ITER need to be re- examined in light of these newly-found torque and plasma rotation dependencies.

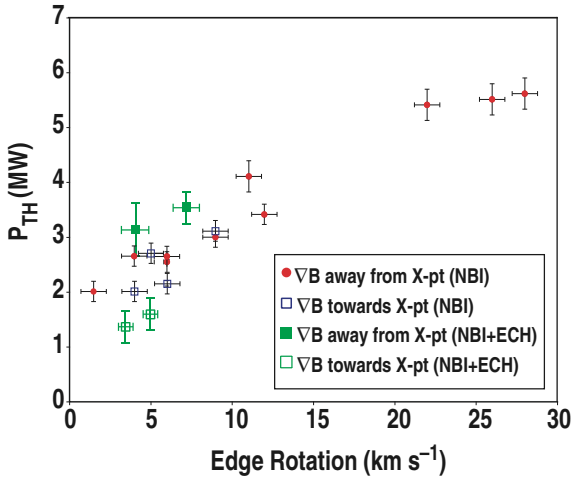

Fig. 9.3. The H-mode threshold power as a function of edge toroidal velocity. The toroidal velocity is measured 1 cm from the separatrix, inside the plasma. The dependence is shown for both USN and LSN plasmas. DIII-D.

9.2. EFFECTS OF TOROIDAL ROTATION ON QH-MODE OPERATION IN DIII-D

9.2.1. Introduction

Quiescent H-mode (QH-mode) was originally discovered in DIII-D [50-52]. It is an advanced confinement mode of operation without ELMs, a very important goal for ITER. Originally, QH-mode was achieved only with counter-Ip neutral beam injection (NBI), that is, injecting the toroidal NBI torque in the opposite direction to the plasma current,

resulting in a plasma with toroidal rotation in this same direction. Subsequently, QH-mode has been experimentally found and investigated on ASDEX-U [53,54], JT-60U [55,56], and JET [54]. There has been a growing indication that the toroidal rotation, or rotation shear is playing a key role in achieving QH-mode [57].

In DIII-D the counter rotation requirement has been systematically pushed back until in 2008 a QH-mode was achieved with co-Ip toroidal rotation throughout the plasma. This is an important demonstration for burning plasmas, that there now clearly exists such an ELM-free mode with varied toroidal rotation.

Here, we highlight the present status of QH-mode research in DIII-D, and describe the achievement of QH-mode with co-rotation this year.

Additional details will appear in the publication cited in Appendix B.15.

9.2.2. Achievement of QH-mode with Varied NBI Torque and Toroidal Rotation

QH-mode plasmas in DIII-D with co plus counter neutral beam injection have demonstrated active control of the edge pedestal that can be used to optimize the edge conditions in future burning plasma devices such as ITER. Burning plasmas impose significant, conflicting constraints on the edge pedestal. To maximize fusion power, H-mode operation is preferred, with an edge pedestal pressure which is as high as possible. However, to eliminate damage to divertor components caused by impulsive heat loads due to Edge Localized Modes (ELMs). ELMs must be eliminated by limiting the edge pressure to a value below that set by the peeling-ballooning mode stability limit. In addition, density control and helium ash removal demand sufficient edge particle transport; ELM-induced particle transport could provide this were it not for the impulsive heat load problem. ELM-free QH-mode plasmas have demonstrated that all these requirements can be met simultaneously in discharges which operate with constant density and radiated power [50].

We have achieved QH-mode operation over a continuous range of input torque from all counter-injection to near balanced injection. As is illustrated in Fig. 9.5, experiments show that altering the torque input to QH-mode plasmas allows continuous adjustment of the pedestal density, pressure and particle transport over a range of about a factor of 2 while maintaining the ELM-free state. This active control capability allows operation near but below the ELM stability boundary with pedestal densities up to about one-half the Greenwald density [58]. In addition, as is shown in Fig. 9.5, we have now achieved QH-mode operation with all co-injection in discharges exhibiting rapid co-rotation in the edge pedestal region.

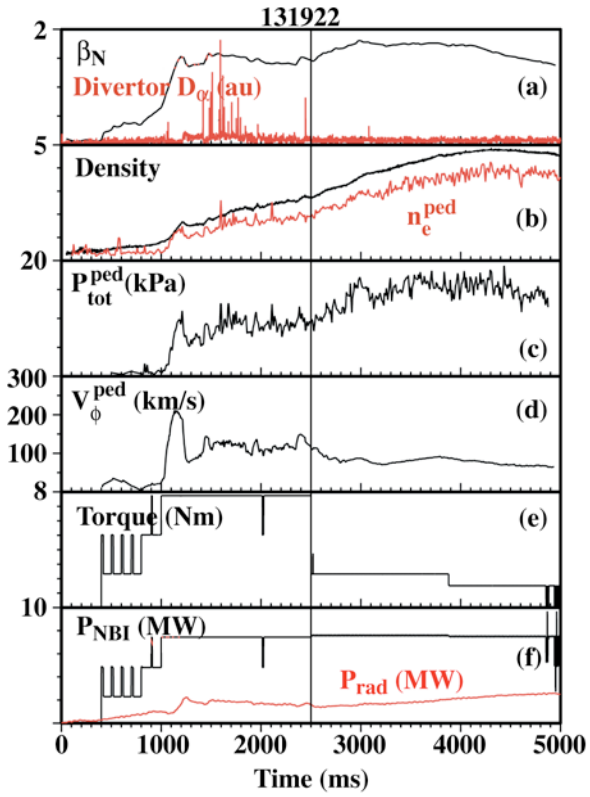

Fig. 9.4. Time history of QH-mode shot showing increase in stored energy (β_N), pedestal density and pedestal pressure as input torque and edge rotation are reduced. (a) Normalized beta and divertor D_α signal, (b) line averaged and pedestal density, (c) total pedestal pressure, (d) pedestal toroidal rotation speed, (e) NBI input torque, (f) NBI input power and total radiated power. For the direction of the plasma current used here, positive rotation values in (d) and positive torque values in (e) are in the counter direction. DIII-D.

Figure 9.5 also shows that these shots have all the usual QH-mode features: (1) ELM-free operation with constant density and radiated power, (2) H-mode level of confinement including the usual H-mode edge pedestal, and (3) enhanced edge particle transport due to the edge harmonic oscillation (EHO) mode. The operational recipe for these plasmas is quite similar to that used for QH-modes with counter injection. Low density operation using divertor cryopumping was one key factor. A second technique employed was feedback control of the neutral beam power to hold normalized beta β_N constant at 1.7 after the L-to-H transition; this produces the neutral beam power waveform shown in Fig. 9.5. Operationally, this recipe produced large toroidal rotation speeds in the edge pedestal of up to 200 km/s. The magnitude of this rotation speed is approximately twice that seen in counter injected QH-mode plasmas of similar shape and with similar torque input.

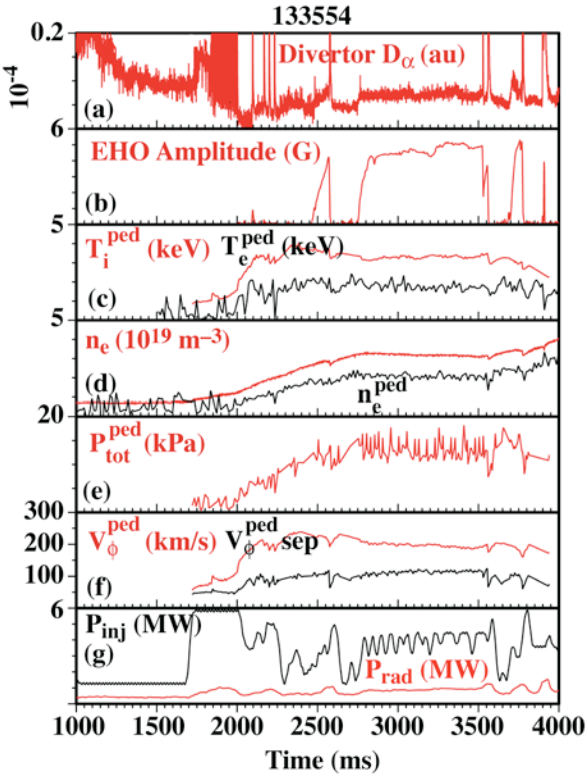

Fig. 9.5. Time history of QH-mode shot with strong co-rotation. (a) Divertor D_α emission, (b) amplitude of oscillating magnetic field associated with EHO, (c) pedestal electron and ion temperature, (d) line averaged and pedestal electron density, (e) total pedestal pressure, (f) pedestal and separatrix toroidal rotation, (g) NBI input power and total radiated power. For the direction of the plasma current used for this shot, positive rotation values in (f) are in the co-direction. Scale in (a) is chosen so that the increase in the D_α when the EHO turns on can be seen; this demonstrates the increase in particle transport caused by the EHO. Peak ELM amplitude is ~20 times the maximum scale used in (a). DIII-D.

10. IMPLICATIONS FOR ITER

10.1. INTRODUCTION

Here we provide present, preliminary conclusions from the JOULE experiments of 2008 regarding rotation, and its impact for ITER. For rotation magnitudes we can only give order of magnitude estimates, here specified by factors of 3. A great deal of data must still be analyzed, and further experiments will be carried out and the projections continually tested.

10.2. TOROIDAL ROTATION IN ITER.

A prediction for the magnitude of intrinsic rotation in ITER based on the scalings derived from present day devices can be made. One measure of the significance of the toroidal velocity is to scale it to the Alfven velocity, V_A. For ITER comparison, using the initially specified inductive scenarios, a velocity of 100km/sec is approximately 2% of V_A, and a rotation frequency of approximately 2 kHz.

Intrinsic rotation clearly exists at $\beta_N \sim 2$. If we use the present intrinsic rotation database scaling to project to ITER we obtain a value of ~ 300 km/sec, in the co-Ip direction. This value can be significant for stability, large enough possibly to stabilize the RWM, and raise the threshold for NTM onset. The present experimental issue is the effect of MHD modes, including NTMs, on the momentum diffusivity. If these modes are actively stabilized in the target $\beta_N \sim 2$ operation in ITER, for example with ECCD, then there is reason to accept the scaling projection that has predominantly come from lower β_N operation in present devices. A second issue is confidence in the size scaling inherent in this projection. Cross-machine experiments on intrinsic rotation must continue, especially involving JET and JT-60U, the largest operating tokamaks.

Toroidal rotation induced by rf has been observed this year in two frequency regimes, Mode Conversion Flow Drive (MCFD) in the ICRF and due to Lower Hybrid Current Drive (LHCD) in the LH frequency regime. These are both emerging areas of study, both experimentally and theoretically. ITER will initially have an ICRF system, and upgrade plans call for a LH system. The MCFD results are in the range predicted by present theory. Projecting to the ITER ICRF system gives a velocity of ~ 100 km/sec, again significant for stability. The FY2008 experiment produced a co-Ip MCFD rotation, so this effect is presumably additive to the ITER intrinsic rotation. The LHCD-driven flow is yet to have detailed theoretical explanation, although a simple physical model appears to explain the phenomenon. A theory will no doubt be forthcoming and ITER projections can be made. This velocity was found to be in the counter-Ip direction, so when coupled

with intrinsic rotation it may be useful to create localized velocity shear, for confinement and stability improvement.

We note that ITER will have a NBI system that will inject toroidal torque. ITER modeling assuming that the momentum diffusivity will be equal to the ion thermal energy diffusivity gives a projected toroidal velocity of ~ 30 km/sec, well below the apparent potential of the above mechanisms. This modeling does not include the momentum pinch, verified by all three JOULE facilities in past or present experiments. The pinch could enhance the NBI-driven toroidal velocity by a factor of 2, possibly. So it is very important to continue to understand the momentum transport, diffusion and pinch effects, both experimentally and theoretically to know if the ITER NBI-driven velocity could contribute to stability and confinement issues, or will be only a perturbation to the other flow generation possibilities.

10.3. SINKS IN ITER

It is understood that resonant magnetic perturbations due to error fields must be minimized in ITER. The experiments are ongoing to specify tolerable bounds for such error fields. JOULE experiments in 2008 have shown that the plasma will be more sensitive to resonant error fields at low rotation.

Nonresonant magnetic error fields drag down the rotation speed in a rapidly rotating plasma in a manner consistent with a torque that agrees with predictions from the neoclassical toroidal viscosity (NTV) theory. ITER is planning to use perturbation coils for ELM control that will produce a significant amount of NTV-induced torque. It is very important to continue experimental understanding of NTV and its impact upon momentum confinement. At low rotation, NTV can produce a nonzero, offset velocity, in the counter-Ip direction, i.e. opposite to the intrinsic rotation in H-mode and to the NBI-driven direction in DIII-D. It is important to do experiments on the combined application of NTV to intrinsically rotating plasmas, to RF-flow driven plasmas and to NBI-driven plasmas to be able to project the impact of the ELM control coils in ITER.

10.4. OTHER ROTATION EFFECTS IN ITER

A major issue for ITER is the L-H power threshold. It appears that at low rotation the threshold is reduced, in plasmas where the rotation is controlled with NBI torque variation. Ostensibly this is good news for ITER, but this must be explored further, and compared with a large amount of data on RF heated H-mode power thresholds, which are in the intrinsic rotation domain already.

Local velocity shear continues to be found to affect local transport. The ability to generate toroidal velocity locally in ITER with RF may provide a useful tool to reduce transport, that is, produce a transport barrier. Coupled with importance of velocity shear,

however, is that of magnetic shear. Future work is needed to determine how these effects impact transport of the electrons and/or ions. At present, we do not have the predictive capability to determine how these effects would project to ITER.

ACKNOWLEDGMENT

This is a report of work supported by the U.S. Department of Energy under Cooperative Agreement No. DE-FC02-04ER54698, DE-AC02-76CH03073 and DE-FC02-99ER54512.

REFERENCES

[1] B.P. Leblanc, *et al.*, Phys. Rev. Lett. **82**, 331 (1999).

[2] J.E. Rice, *et al.*, Nucl. Fusion **39**, 1175 (1999).

[3] W.D. Lee, *et al.*, Phys. Rev. Lett. **91**, 205003 (2003).

[4] J.C. Wright, *et al.*, Phys. Plasmas **11**, 2473 (2004).

[5] J.R. Myra and D.A. D'Ippolito, Phys. Plasmas **9,** 3867 (2002).

[6] J.E. Rice, *et al.*, Nucl. Fusion **47**, 1618 (2007), and references therein.

[7] A. Scarabosio, *et al.*, Plasma Phys. Control. Fusion **48**, 663 (2006).

[8] B.P. Duval, *et al.*, Phys. Plasmas **15**, 056113 (2008).

[9] J.S. deGrassie, *et al.*, Phys. Plasmas **14**, 056115-1 (2007), and references therein.

[10] B.J. Green, Plasma Phys. Control. Fusion **45**, 687 (2003).

[11] J.E. Rice, *et al.*, Nucl. Fusion **41**, 277 (2001).

[12] I.H. Hutchinson, *et al.*, Phys. Rev. Lett. **84**, 3330 (2000).

[13] R.E. Waltz, *et al.*, Phys. Plasmas **14**, 122507 (2007).

[14] W.M. Solomon, *et al.*, Plasma Phys. Control. Fusion **49**, B313 (2007).

[15] J.S. deGrassie, *et al.*, Phys. of Plasmas **11**, 4323 (2004).

[16] J.S. deGrassie, *et al.*, in *Proceedings of the 20th International Conference on Plasma Physics and Controlled Nuclear Fusion Research 2004*, Vilamoura, Portugal (IAEA, Vienna, 2005), Paper IAEA-CN-116-EX/6-4Rb.

[17] Peeters, *et al.*, Phys. Rev. Lett. **98** (2007) 265003.

[18] Hahm, et al, Phys. Plasmas **14**, (2007) 072302.

[19] Shaing, Phys. Plasmas **8**, 193 (2001).

[20] Diamond, *et al.*, Phys. Plasmas **15**, 021303 (2008).

[21] W.D. Lee, *et al.*, Phys. Rev. Lett. **91**, 205003 (2003).

[22] A.-Ince-Cushman, *et al.*, Rev. Sci. Instrum. **79**, (2008), accepted for publication.

[23] W. Zhu, *et al.*, Phys. Rev. Lett. **96**, 225002 (2006).

[24] A. Cole, C. Hegna, and J. Callen, Phys. Rev. Lett. **99**, 065001 (2007).

[25] A. Cole, C. Hegna, and J. Callen, Phys. Plasmas **15**, 056102 (2008).

[26] H.R. Wilson, Plasma Phys. Controlled Fusion **38**, A149 (1996).

[27] H. Reimerdes, *et al.*, Plasma Phys. Control. Fusion **49** B349 (2007).

[28] M. Becoulet, 11th ITPA-MHD/IEA Large Tokamak Workshop, Feb 25-29, 2008.

[29] D.K. Mansfield, *et al.*, "Transition to ELM-free improved H-mode by lithium deposition on NSTX graphite divertor surfaces," in proceedings of the 18th PSI meeting, Toledo, Spain May 26th-30th, 2008, paper O-28; accepted for publication in J. Nucl. Mater.

[30] R.J. La Haye, *et al.*, Phys. Fluids B **4**, 2098 (1992).

[31] A.M. Garofalo, *et al.*, Nucl. Fusion **47**, 1121 (2007).

[32] A.H. Boozer, Phys. Rev. Lett. **86**, 5059 (2001).

[33] R. Fitzpatrick, Nucl. Fusion **33**, 1049 (1993).

[34] ITER Physics Basis, Nucl. Fusion **39**, 2137 (1999).

[35] McDermott TTF Boulder.

[36] C.S. Chang and S. Ku, Phys. Plasmas **15**, 62510 (2008).

[37] R.E. Waltz, *et al.,* Phys. Plasmas **14**, 122507 (2007).

[38] L.L. Lao, *et al.,* Fusion Sci. Technol. **48**, 968 (2005).

[39] G.D. Porter, *et al.,* Phys. Plasmas **5**, 1410 (1998).

[40] K.C. Shaing, Phys. Plasmas **8**, 193 (2001).

[41] P.H. Diamond, *et al.,* Phys. Plasmas **15**, 012303 (2008).

[42] E.J. Strait, *et al.*, Phys. Plasmas **14**, 056101 (2007.

[43] B. Hu and R. Betti, Phys. Rev. Lett. **93**, 105002 (2004).

[44] A.H. Boozer, Phys. Rev. Lett. **86**, 5059 (2001).

[45] A.C. Sontag, *et al.*, Nucl. Fusion **47**, 1005 (2007).

[46] R. Fitzpatrick, Phys. Plasmas **9**, 3459 (2002).

[47] B. Hu, *et al.*, Phys. Plasmas **12**, 057301 (2005).

[48] Austin, *et al.*, Phys. Plasmas **13**, 082502 (2006).

[49] R.E. Waltz, *et al.*, Phys. Plasmas **13**, 052301 (2006).

[50] K.H. Burrell, *et al.*, Phys. Plasmas **12**, 056121 (2005).

[51] K.H. Burrell, *et a*l., Bull. Am. Phys. Soc. **44**, 127 (1999).

[52] K.H. Burrell, *et al.*, Phys. Plasmas **8**, 2153 (2001).

[53] W. Suttrop, *et al.*, Plasma Phys. Control. Fusion **45**, 1399 (2003).

[54] W. Suttrop, *et al.*, Nucl. Fusion **45**, 721 (2005).

[55] Y. Sakamato, *et al.*, Plasma Phys. Control. Fusion **46**, A299 (2004).

[56] N. Oyama, *et al.*, Nucl. Fusion **45**, 871 (2005).

[57] P.B. Snyder, *et al.*, Nucl. Fusion **47**, 961 (2007).

[58] M. Greenwald, *et al.*, Nucl. Fusion **28**, 2199 (1988).

APPENDIX A: FY08 JOULE MILESTONE PROGRESS

FY2008 Joule Milestone Progress
C=C-Mod N=NSTX D=DIII-D

Not in priority order

Numbers for linkages to others

Area		exp	Title	links	exp	Q2 exps	Q3 exps	Q4 exps
IA Sources: Intrinsic	C	1	Intrinsic rotation database continuation	5,6	1	Multiple exps	Multiple exps	
	C	2	Intrinsic rotation profile evolution	5,13,14	2	Multiple exps	Multiple exps	
	C	3	Rotation in LHCD plasmas, (and possibly MCEH plasmas)	6	3	MP523	MP523 MP497	
	C	4	Rotation inversion vs ne, Ip - in limiter/divertor plasmas		4		MP535a	
	D	5	Intrinsic rotation at high normalized pressure using balanced NBI	1,2	5	02-03	02-03	
	D	6	Expand DIII-D intrinsic rotation database, especially shape effects, SOL flows	1,3	6		02-06	
	D	7	Measure edge turbulent momentum transport (relates to boundary condition)	8	7		02-06	
	D	44	Measure intrinsic rotation in bulk ion Hydrogen discharges.	1,6	44			
	N	8	Mean and oscillating turbulent flows using Doppler reflectometry	7	8			
IB Sources: Driven	D	9	Measure off-axis NBCD and validate NBCD physics		9	55-02	55-01	55-03
	D	10	Affect of Alfven Eigenmodes on NBCD and fast ion profileÜ		10		57-01	
	D	43	NBI torque profile	9,11	43			
II Momentum Transport	N	11	Perturbative modulation of core rotation using beam blips; diffusion and pinch.	14,2	11	XP820		
	N	12	Non-core perturbative modulation of rotation using n=1 magnetic braking blips	19,20	12	XP813		
	C	13	Momentum transport, locked/unlocked	2,20,22,12	13		MP550	
	C	2	Intrinsic rotation profile evolution	11,14	2		Multiple exps	
	D	14	NBI modulated transport at low rotation with balanced NBI (piggybacks)	2	14			
	C	42	Momentum impulse due to rapid shape change (SSEP)	2,20,22	42	MP537	MP537	
IIIA Sinks: non-resonant b	N	15	Comparison of NTV among tokamaks	18	15	XP804		
	N	16	Island-induced NTV		16			
	D	17	Test Two vs. One row ELM-suppression coils for ITER, n=3		17	03-01		
	D	18	Test NTV offset rotation, and collisionality effect, with applied n=3	15,21	18	02-01 02-02	02-12	02-12
IIIB Sinks: resonant b	C	19	Intrinsic rotation with n=1 braking	12	19	MP478	MP550	
	D	20	Resonant n=1 braking and error field thresholds	12,13	20	02-05		02-05
IV b Penetration	D	21	RMP screening or amplification dependence upon rotation	18	21			03-13
	C	22	Rotation in H-modes and locked modes	13	22		MP550	
V Boundary Condition	C	23	Er well spatial structure and parameter scaling		23	MP538	MPs 531/32/38	
	D	7	Measure edge turbulent momentum transport	8	7		02-06	
	D	5-7	included in these experiments		5-7			
VI Main ion rotation/ Neoclassical theory	C	24	Edge ion rotation in helium plasmas (related to boundar condition)	25	24	MP519	defer	
	D	25	Main ion rotation studies (helium)	24,26	25			
	N	26	Poloidal rotation studies; relation to neoclassical theory	25	26			
VIIA Rotation and Stability - RWM	D	27	Measure RWM damping by plasma rotation	29	27		14-03	
	D	28	Demonstrate RWM feedback stabilization at low rotation		28	14-01		
	N	29	RWM stabilization and damping	27	29	XP805		
	N	30	Active RWM feedback stabilization optimization		30			
VIIB Rotation and Stability - NTM	N	31	Rotation dependence of 2/1 NTM thresholds	33	31	XP801 XP810		
	N	32	Studies of the 3/2 NTM; rotation and rampdown	34	32			
	D	33	Effect of rotation on NTM beta limits	31	33		02-08	
	D	34	NTM 3/2 mode stability at low rotation	32	34		02-08	

Not in priority order

FY2008 Joule Milestone Progress
C=C-Mod N=NSTX D=DIII-D

Numbers for linkages to others

VIII Impact of Rotation on Confinement	N	35	Dependence of energy and impurity transport upon rotation (n=3 modification)		35	XP812		
	D	36	Changes in confinement with rotation		36		53-02	
	C	37	Rotation during sawteeth	33	37	MP520		
IX Other Rotation Effects that impact ITER	D	38	Dependence of the L->H power threshold upon rotation		38	53-01		35-01 (H2)
	D	39	QH mode at low small plasma rotation		39	03-02		
	N	40	Dependence of the L->H power threshold upon rotation through n=3 braking		40			
	C	1	Intrinsic rotation database continuation		1			
	D	41	Effect of Core Rotation on SOL flows		41	56-01		21-01, 56-01
	D	42	QH mode in co-rotating plasmas	39	42		03-10	

C-Mod: List of experimental mini proposals (MPs) and links to run date where applicable. https://www.psfc.mit.edu/research/alcator/program/cmod_runs.php?miniproposals&sort=date_filed&dir=desc

NSTX: List of experimental plans (XPs) with files that describe the XPs listed here. http://nstx.pppl.gov/DragNDrop/XP_Folder/Approved_XPs/FY08/

DIII-D: List of experiments by date with a link to the mini proposals describing the experiments. The experimental number used in this spreadsheet is comprised of the numbers in columns 1 and 2 of the weblink. https://diii-d.gat.com/diii-d/Explist08

APPENDIX B: PUBLICATIONS FROM 2008 RELATED TO THE FES 2008 JOINT JOULE MILESTONE

1. Y. Lin, *et al.*, submitted to Phys. Rev. Lett. (2008).
2. A. Ince-Cushman, *et al.*, Phys Rev. Lett, accepted for publication (2008).
3. J.E. Rice, *et al.*, Proc. 22nd Fusion Energy Conf., Geneva, Switzerland, (IAEA, Vienna), 2008.
4. J.E. Rice, *et al.*, Plasma Phys. Control. Fusion **50**, (2008), to be published.
5. W.M. Solomon, *et al.*, Phys. Rev. Lett. **101**, 065004 (2008).
6. W.M. Solomon, *et al.*, Proc. European Physical Society Meeting, 2008.
7. S. M. Kaye, *et al.*, Proc. 22nd Fusion Energy Conf., Geneva, Switzerland, (IAEA, Vienna), 2008.
8. A. M. Garofalo, *et al.*, Phys. Rev. Lett., **101**, to be published (2008).
9. R. Kaita, *et al.*, Proc. 22nd Fusion Energy Conf., Geneva, Switzerland, (IAEA, Vienna), 2008.
10. H. Reimerdes, *et al.*, Proc. 22nd Fusion Energy Conf., Geneva, Switzerland, (IAEA, Vienna), 2008.
11. J.S. deGrassie, *et al.*, Proc. 22nd Fusion Energy Conf., Geneva, Switzerland, (IAEA, Vienna), 2008.
12. R.J. Buttery, *et al.*, Proc. 22nd Fusion Energy Conf., Geneva, Switzerland, (IAEA, Vienna), 2008.
13. S. Sabbagh, *et al.*, Proc. 22nd Fusion Energy Conf., Geneva, Switzerland, (IAEA, Vienna), 2008.
14. G.R. Mckee, *et al.*, Proc. 22nd Fusion Energy Conf., Geneva, Switzerland, (IAEA, Vienna), 2008.
15. K.H. Burrell, *et al.*, Proc. 22nd Fusion Energy Conf., Geneva, Switzerland, (IAEA, Vienna), 2008.